



**HAL**  
open science

# Copper (II) Heterocyclic Thiosemicarbazone Complexes as Single-Source Precursors for the Preparation of Cu<sub>9</sub>S<sub>5</sub> Nanoparticles: Application in Photocatalytic Degradation of Methylene Blue

Adrien Yepseu, Thomas Girardet, Linda Nyamen, Solenne Fleutot, Kevin Ketchemen, Franck Cleymand, Peter Ndifon

## ► To cite this version:

Adrien Yepseu, Thomas Girardet, Linda Nyamen, Solenne Fleutot, Kevin Ketchemen, et al.. Copper (II) Heterocyclic Thiosemicarbazone Complexes as Single-Source Precursors for the Preparation of Cu<sub>9</sub>S<sub>5</sub> Nanoparticles: Application in Photocatalytic Degradation of Methylene Blue. *Catalysts*, 2022, 12, 10.3390/catal12010061 . hal-03668302

**HAL Id: hal-03668302**

**<https://hal.science/hal-03668302>**

Submitted on 14 May 2022

**HAL** is a multi-disciplinary open access archive for the deposit and dissemination of scientific research documents, whether they are published or not. The documents may come from teaching and research institutions in France or abroad, or from public or private research centers.





L'archive ouverte pluridisciplinaire **HAL**, est destinée au dépôt et à la diffusion de documents scientifiques de niveau recherche, publiés ou non, émanant des établissements d'enseignement et de recherche français ou étrangers, des laboratoires publics ou privés.



Distributed under a Creative Commons Attribution 4.0 International License

Article

# Copper (II) Heterocyclic Thiosemicarbazone Complexes as Single-Source Precursors for the Preparation of Cu<sub>9</sub>S<sub>5</sub> Nanoparticles: Application in Photocatalytic Degradation of Methylene Blue

Adrien P. Yepseu <sup>1,2</sup>, Thomas Girardet <sup>2</sup>, Linda D. Nyamen <sup>1</sup>, Solenne Fleutot <sup>2</sup>, Kevin I. Y. Ketchemen <sup>1</sup>, Franck Cleymand <sup>2,\*</sup> and Peter T. Ndifon <sup>1,\*</sup>

<sup>1</sup> Department of Inorganic Chemistry, Faculty of Science, University of Yaounde I, Yaounde P.O. Box 812, Cameroon; yepseuadrien@gmail.com (A.P.Y.); line84fr@yahoo.fr (L.D.N.); kevinketchemen@yahoo.fr (K.I.Y.K.)

<sup>2</sup> Institut Jean Lamour UMR 7198 CNRS, Université de Lorraine Campus Artem, 2 Allée André Guinier, 54000 Nancy, France; thomas.girardet@univ-lorraine.fr (T.G.); solenne.fleutot@univ-lorraine.fr (S.F.)

\* Correspondence: franck.cleymand@univ-lorraine.fr (F.C.); pndifon@facsciences-uy1.cm (P.T.N.)

**Abstract:** In this study, two copper(II) complexes, [Cu(C<sub>6</sub>H<sub>8</sub>N<sub>3</sub>S<sub>2</sub>)<sub>2</sub>]Cl<sub>2</sub> (1) and [Cu(C<sub>7</sub>H<sub>10</sub>N<sub>3</sub>S<sub>2</sub>)<sub>2</sub>]Cl<sub>2</sub>·H<sub>2</sub>O (2), were synthesized from 2-(thiophen-2-ylmethylene)hydrazine-1-carbothioamide (L<sub>1</sub>H) and 2-(1-(thiophen-2-yl)ethylidene)hydrazine-1-carbothioamide (L<sub>2</sub>H) respectively and characterized using various spectroscopic techniques and elemental analyses. The as-prepared complexes were used as single-source precursors for the synthesis of oleylamine-capped (OLA@Cu<sub>x</sub>S<sub>y</sub>), hexadecylamine-capped (HDA@Cu<sub>x</sub>S<sub>y</sub>), and dodecylamine-capped (DDA@Cu<sub>x</sub>S<sub>y</sub>) copper sulphide nanoparticles (NPs) via the thermolysis method at 190 °C and 230 °C and then characterized using powder X-ray diffraction (p-XRD), UV-visible spectroscopy, transmission electron microscopy (TEM), and scanning electron microscopy (SEM). The p-XRD diffraction patterns confirmed the formation of crystalline rhombohedral digenite Cu<sub>9</sub>S<sub>5</sub> with the space group R-3m. The TEM images showed the formation of nanoparticles of various shapes including hexagonal, rectangular, cubic, truncated-triangular, and irregularly shaped Cu<sub>9</sub>S<sub>5</sub> nanomaterials. The SEM results showed aggregates and clusters as well as the presence of pores on the surfaces of nanoparticles synthesized at 190 °C. The UV-visible spectroscopy revealed a general blue shift observed in the absorption band edge of the copper sulphide NPs, as compared to bulk Cu<sub>x</sub>S<sub>y</sub>, with energy band gaps ranging from 2.52 to 3.00 eV. Energy-dispersive X-ray spectroscopy (EDX) confirmed the elemental composition of the Cu<sub>9</sub>S<sub>5</sub> nanoparticles. The nanoparticles obtained at 190 °C and 230 °C were used as catalysts for the photocatalytic degradation of methylene blue (MB) under UV irradiation. Degradation rates varying from 47.1% to 80.0% were obtained after 90 min of exposure time using only 10 mg of the catalyst, indicating that Cu<sub>9</sub>S<sub>5</sub> nanoparticles have potential in the degradation of organic pollutants (dyes).

**Keywords:** heterocyclic thiosemicarbazone copper (II) complexes; thermolysis; copper sulphide nanoparticles; optical properties; photocatalysts



**Citation:** Yepseu, A.P.; Girardet, T.; Nyamen, L.D.; Fleutot, S.; Ketchemen, K.I.Y.; Cleymand, F.; Ndifon, P.T. Copper (II) Heterocyclic Thiosemicarbazone Complexes as Single-Source Precursors for the Preparation of Cu<sub>9</sub>S<sub>5</sub> Nanoparticles: Application in Photocatalytic Degradation of Methylene Blue. *Catalysts* **2022**, *12*, 61. <https://doi.org/10.3390/catal12010061>

Academic Editors: Salam Titinchi and Hanna Abbo

Received: 26 November 2021

Accepted: 27 December 2021

Published: 6 January 2022

**Publisher's Note:** MDPI stays neutral with regard to jurisdictional claims in published maps and institutional affiliations.



**Copyright:** © 2022 by the authors. Licensee MDPI, Basel, Switzerland. This article is an open access article distributed under the terms and conditions of the Creative Commons Attribution (CC BY) license (<https://creativecommons.org/licenses/by/4.0/>).

## 1. Introduction

In recent decades, there has been an increasing interest in semiconductor metal chalcogenide nanocrystals (NCs) due to their various applications in nanoscience and nanotechnology [1,2]. Their unique properties make them a subject of intense research and are strongly influenced by morphology, phase, and surface properties [1–4]. Amongst metal chalcogenides, copper sulphide, which is a p-type semiconductor with a tuneable band-gap ranging from 1.2 eV to 2.0 eV, has become highly sought after due to its wide range of stoichiometric compositions and phases. These phases vary from the copper-rich chalcocite

phase ( $\text{Cu}_2\text{S}$ ) to the copper-deficient phases (covellite ( $\text{CuS}$ ), anilite ( $\text{Cu}_{1.75}\text{S}$ ), digenite ( $\text{Cu}_{1.8}\text{S}$ ), and djurleite ( $\text{Cu}_{1.96}\text{S}$ )) [5–9]. Copper-containing nanomaterials have been shown to possess potential applications in solar cells [5], photocatalysis [6], supercapacitors [10], nanometre-scale switches, and high-capacity cathode materials in lithium secondary batteries, superconductor, thermoelectric cooling material, and solar-energy absorption [11,12]. These varied applications of copper sulphide semiconductor materials stem from their unique optical, electronic, and photocatalytic properties that are influenced by their morphology, their stoichiometric composition, and their crystalline phases, which are tuneable by various reaction parameters such as their capping agent, the nature of their precursor, and their reaction temperature [7–9,13]. Capping agents stabilize the surface of copper sulphide to prevent agglomeration and to obtain monodisperse nanoparticles (NPs) [14,15]. However, controlling the phase and the morphology of copper sulphide NPs has been difficult to achieve.

Significant efforts have been devoted to phase-controlled synthesis of copper sulphide NPs [13–15]. Several methods have been developed for structure-controlled synthesis of copper sulphide nanoparticles, including microwave irradiation [16], solvothermal [17], and thermolysis of a single-source precursor [18,19]. Among these synthetic routes, the thermolysis of single-source precursors has been shown to yield high-quality nanoparticles due to the presence of the preformed metal–sulphur bond in the molecule, which can control the chemical composition and physical properties of the as-prepared metal chalcogenide NPs [15,20–23]. This method regulates the particle size and shape by varying reaction conditions such as temperature, precursor concentration, and capping group [7,8,24]. The choice of precursors plays an important role on the morphology and phase of copper sulphide NPs [16]. Thermolysis of dithiocarbamates [6], xanthates [25], dithiolates [26], and thiobiuret [27] compounds have been explored as single-source precursors for the preparation of copper sulphide nanoparticle. Despite the various reports on the synthesis of copper sulphide NPs, the effects of capping agents on crystallinity, phase, size, shape, optical, and photocatalytic properties have not been fully explored. Recently, our group reported the use of thiourea Cu(II) complexes, N-morpholine-N-benzoylthioureatocopper(II), and N-pyrrolidine-N-benzoylthioureatocopper(II) complexes as single-source precursors for the preparation of copper sulphide NPs with various morphologies [8,9], and our results indicate that the formation of the roxbyite phase ( $\text{Cu}_{1.75}\text{S}$ ) was solvent and temperature dependent [9]. Studies have also reported the use of Cu(II) complexes for the photodegradation of organic dyes in aqueous solution [28,29].

Copper(II) heterocyclic thiosemicarbazone complexes have been extensively studied for their antimicrobial, anticancer, and antiviral properties [30–35]. However, little attention has been paid to their use as a single source precursor for the preparation of  $\text{Cu}_x\text{S}_y$  nanoparticles. Heterocyclic thiosemicarbazones are chelating ligands with the ability to form air-stable and less toxic complexes possessing the pre-formed metal-sulfur (M-S) bonds. We hereby report on the synthesis of two heterocyclic thiosemicarbazone copper (II) complexes and their use as single-source precursors to prepare  $\text{Cu}_x\text{S}_y$  NPs at 190 °C and 230 °C, using oleylamine (OLA), hexadecylamine (HDA), and dodecylamine (DDA) as capping agents. We also report on the use of OLA-capped  $\text{Cu}_x\text{S}_y$ , HDA-capped  $\text{Cu}_x\text{S}_y$ , and DDA-capped  $\text{Cu}_x\text{S}_y$  NPs obtained as photocatalysts for the degradation of methylene-blue (MB) dye under UV irradiation.

## 2. Results and Discussion

### 2.1. Characterisation of the Ligands and Complexes

The ligands and their corresponding Cu(II) complexes were obtained in appropriate yields, and microanalysis confirmed their purity. All the compounds were coloured, air-stable, and soluble in dimethyl sulphoxide (DMSO). The molar conductance values of the complexes recorded in the DMSO as a solvent for complex 1 ( $[\text{Cu}(\text{C}_6\text{H}_8\text{N}_3\text{S}_2)_2]\text{Cl}_2$ ) and complex 2 ( $[\text{Cu}(\text{C}_7\text{H}_{10}\text{N}_3\text{S}_2)_2]\text{Cl}_2 \cdot \text{H}_2\text{O}$ ), indicating the electrolytic nature of both complexes [36,37].

### 2.1.1. Infrared Study

The bonding mode of the ligands in each Cu (II) complex was determined by comparing the Fourier-transform infrared (FTIR) spectrum of the ligand with that of the corresponding metal complex. The FTIR spectra of the ligands and their corresponding Cu(II) complexes are presented in Figure S1. The FTIR spectra of the free ligands exhibited a band within the range 1582–1595  $\text{cm}^{-1}$  assigned to  $\nu(\text{C}=\text{N})$ . In the spectra of complexes 1 and 2, this band shifted to higher frequencies by ca. 6–16  $\text{cm}^{-1}$  (1602–1608  $\text{cm}^{-1}$ ), suggesting the coordination of the azomethine nitrogen to the central metal atom. In addition, this coordination was supported by the presence of  $\nu(\text{M}-\text{N})$  vibrations at approximately 515–540  $\text{cm}^{-1}$ . In the IR spectra of the ligands, the  $\nu(\text{S}-\text{H})$  band that usually appears at approximately 2570  $\text{cm}^{-1}$  [38,39] was absent while the  $\nu(\text{C}=\text{S})$  bands at 830 and 835  $\text{cm}^{-1}$  were present. These  $\nu(\text{C}=\text{S})$  bands had shifted to lower frequencies by ca. 4–10  $\text{cm}^{-1}$  (820–831  $\text{cm}^{-1}$ ) in the spectra of complexes 1 and 2. This shift was attributed to the thiocarbonyl  $\nu(\text{C}=\text{S})$  stretching and bending modes of vibrations and confirmed the coordination of the sulphur atom to the metal ion (M-S) [38,39]. The band that appeared around 3248  $\text{cm}^{-1}$  in the spectrum of the complex with the ligand ( $\text{L}_2$ ) was attributed to water of crystallisation [38].

### 2.1.2. Thermal Decomposition Studies of Precursors

The TGA curves of complexes (1) and (2) are shown in Figure 1. The thermal decomposition curve of complex 1 showed two decomposition steps. The first decomposition occurred within a temperature range of 211–276  $^{\circ}\text{C}$  with a mass loss of 35.9% (calculated (calc): 36.8%), which corresponded to the degradation of the ligand molecule ( $\text{L}_1$ ) (curve ii in Figure 1). The second decomposition step involved a weight loss of 31.3% (calc: 30.8%) within a temperature range of 276–525  $^{\circ}\text{C}$ , which was attributed to the loss of the organic moiety and chloride (curve v in Figure 1). The final residues comprised copper sulphide and carbon (found: 31.5%; calc: 32.4%) [30,38]. The thermal decomposition curve of complex 2 showed three decomposition steps. The first step between 50  $^{\circ}\text{C}$  and 144  $^{\circ}\text{C}$  corresponds to the loss of a water molecule (found: 3.3%; calc: 3.2%) (curve i in Figure 1). The second decomposition step between 178  $^{\circ}\text{C}$  and 284  $^{\circ}\text{C}$  corresponds to the loss of a ligand ( $\text{L}_2$ ) molecule and a chloride ion (found: 41.6%; calc: 42.5%) (curve iii in Figure 1), while the third decomposition step, which occurred between 305  $^{\circ}\text{C}$  and 530  $^{\circ}\text{C}$  (Found: 21.03%; calc: 20.2%), corresponds to the decomposition of an organic moiety (curve iv in Figure 1). The final residues of 34.07% (calc: 34.1%) were attributed to the mixture of copper sulphide and carbon residue [30,38].

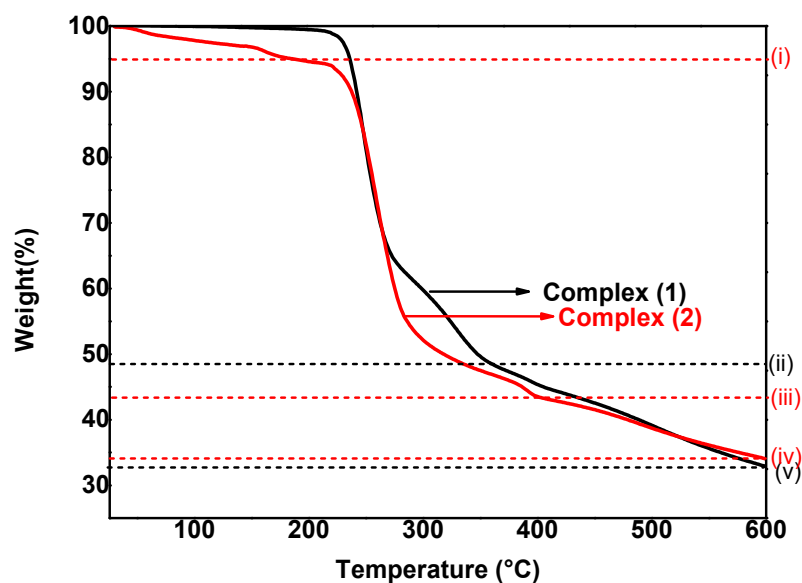


Figure 1. Thermogravimetric analysis (TGA) graph of complexes 1 and 2.



## 2.2. Characterisation of Copper Sulphide Nanoparticles

### 2.2.1. Structural Characterization of $\text{Cu}_x\text{S}_y$ Nanoparticles

The powder X-ray diffraction (p-XRD) patterns of copper sulphide NPs synthesized using complexes 1 and 2 in OLA ( $\text{C}_{18}$ ), HDA ( $\text{C}_{16}$ ), and DDA ( $\text{C}_{10}$ ) at  $190^\circ\text{C}$  are presented in Figure 2. When complex 1 was used as a precursor with OLA, HDA, and DDA as capping agents, the p-XRD patterns (Figure 2I(a–c)) with the lattice planes (0 0 15), (1 0 7), (1 0 10), (0 1 20), and (1 1 15) were indexed to pure rhombohedral digenite  $\text{Cu}_9\text{S}_5$  with space group R-3m. In addition, the diffractogram of copper sulphide NPs synthesized with OLA as capping agents showed extra peaks (denoted \*, Figure 2I(a)) that were attributed to the roxbyite  $\text{Cu}_7\text{S}_4$  phase, (JCPDS: 023-0958). When complex 2 was used, the rhombohedral digenite  $\text{Cu}_9\text{S}_5$  with space group R-3m was also observed with all three capping agents, with no other phases present, which confirmed the phase purity of the  $\text{Cu}_9\text{S}_5$  NPs (Figure 2II(a–c)). The p-XRD results agreed with the reported data for copper sulphide nanostructures synthesized from copper(II) piperidine dithiocarbamate precursors using a single-source precursor route [15,40].

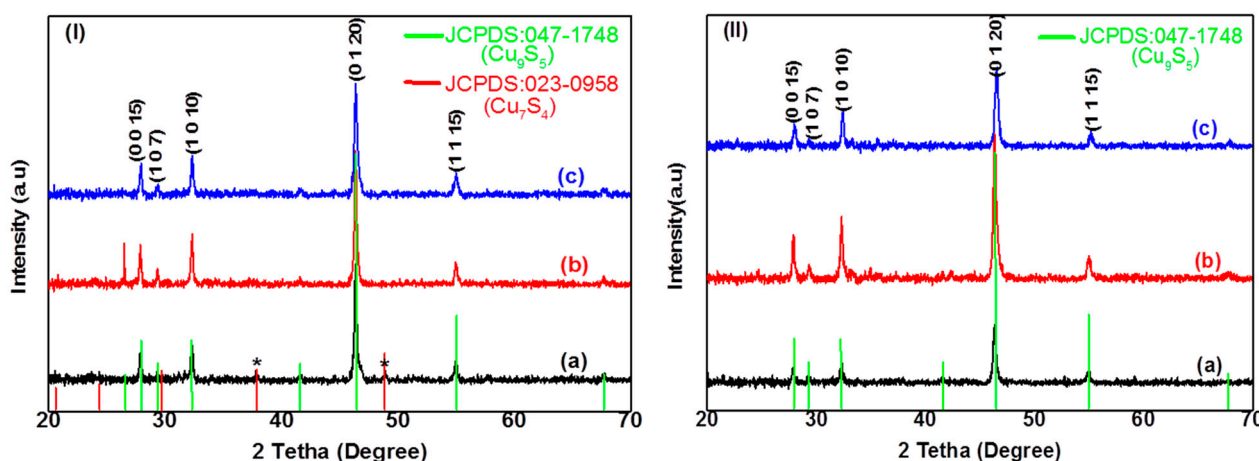


**Figure 2.** p-XRD patterns of  $\text{Cu}_x\text{S}_y$  nanoparticles prepared in (a) OLA, (b) HDA, and (c) DDA at  $190^\circ\text{C}$  using (I) complex 1 and (II) complex 2.

Crystalline nanoparticles were also obtained when the reaction temperature was increased to  $230^\circ\text{C}$  using complexes 1 and 2 as well as all the capping agents (Figure 3). The rhombohedral phase ( $\text{Cu}_9\text{S}_5$ , digenite) was also obtained with the lattice planes (0 0 15), (1 0 7), (1 0 10), (0 1 20), and (1 1 15) (JCPDS: 047-1748). The rhombohedral phase ( $\text{Cu}_9\text{S}_5$ , digenite) has been commonly reported for copper chalcogenide NPs [41].

EDX analysis were performed to confirm the elemental composition of the synthesized  $\text{Cu}_x\text{S}_y$  NPs and results are presented in Figure 4, Tables 1 and 2. The EDX spectra showed the presence of Cu and S, as well as other constituent elements such as C and O, when complexes 1 and 2 were employed as precursors. The presence of the carbon peak was attributed to the capping agents OLA, HDA, and DDA as well as the double-sided carbon tape that had been used for mounting the nanoparticles. The presence of Cu and S indicated the formation of copper sulphide NPs. The Cu/S ratios approximately corresponded to the expected compositions, with a slightly copper-rich stoichiometry in the OLA@ $\text{Cu}_9\text{S}_5$  and the HDA@ $\text{Cu}_9\text{S}_5$  NPs using complex 1. The high percentage of Cu could be attributed to the excessive absorption of copper ions onto the surface of NPs. Similar results were recently obtained by Murendeni et al. [15]. The EDX spectra of the DDA@ $\text{Cu}_9\text{S}_5$  NPs confirmed that the primary elemental constituents of the nanoparticles were copper and sulphur in a molar ratio of 1.83:1 (Cu/S), which agreed with the stoichiometric ratio in the digenite phase. A similar trend was observed for the OLA@ $\text{Cu}_9\text{S}_5$  NPs when complex 2 was used as precursor (Figure S2). The results showed Cu/S ratios that represented sulphur-rich and copper-deficient stoichiometries and thus indicated the nonstoichiometric compositions

in the structures of the samples (Figure S2) of the HDA@Cu<sub>9</sub>S<sub>5</sub> and DDA@Cu<sub>9</sub>S<sub>5</sub> NPs. The presence of oxygen on the EDX spectrum of Cu<sub>9</sub>S<sub>5</sub> NPs prepared in OLA and DDA could be explained by the absorption of oxygen from the air during sample preparation for analysis. The results of the composition of Cu<sub>x</sub>S<sub>y</sub> nanoparticles when OLA, HDA, and DDA were used as capping agents at 230 °C (Figures S3a–c and S4a–c) were comparable to those obtained at 190 °C. A general trend was observed where a decrease in the carbon chain of the primary amine-capping agent (OLA–DDA), C<sub>18</sub>–C<sub>12</sub>, had resulted in alteration of the composition (Cu/S ratio) in the copper sulphide NPs.

### 2.2.2. Morphological Characterisation of Cu<sub>x</sub>S<sub>y</sub> Nanoparticles

The morphology of the synthesized copper sulphide NPs was investigated by TEM analyses, and the results are given in Figures 5 and 6. When OLA (C<sub>18</sub>) was used as a stabilising agent, agglomerated irregularly shaped particles were formed with sizes ranging from 49 to 80 nm using complex 1 as a precursor (Figure 5a). The large particles resulting from the interparticle aggregation were also formed. When the stabilizing agent was changed to HDA (C<sub>16</sub>), a mixture of rectangular and cubic-shaped copper sulphide NPs with sizes ranging from 46 to 134 nm was formed (Figure 5b). When DDA (C<sub>12</sub>) was used, rectangular and irregularly shaped particles with sizes ranging from 53 to 154 nm were produced (Figure 5c). The properties of the capping group had some influence on the size of the nanoparticles through the dynamics of attaching and detaching [42].

The influence of the precursor was studied by replacing complex 1 with complex 2 under similar reaction conditions. A slight difference was observed in the morphologies of the copper sulphide NPs. When OLA was used, agglomerated, shapeless particles were formed with estimated sizes ranging from 32 to 75 nm (Figure 5d). When HDA was used, a mixture of semi-spherical and rectangular particles with estimated sizes of 43–125 nm (Figure 5e) was produced. DDA as a capping agent produced irregular cubic-shaped particles with sizes ranging 23–125 nm (Figure 5f). The morphologies of copper sulphide reported in this work were comparable to those previously reported [4,43].

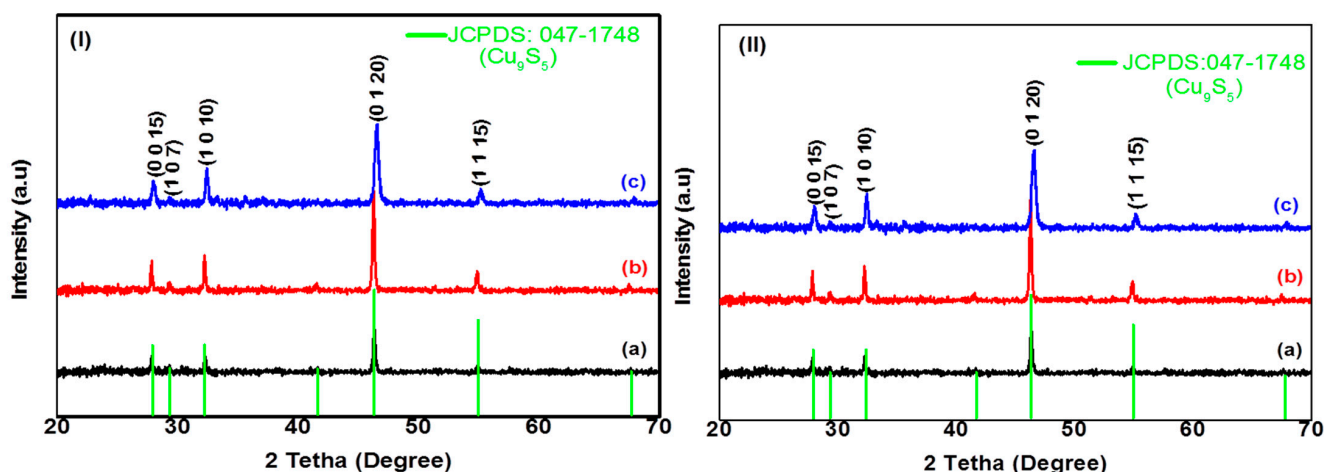


**Figure 3.** p-XRD patterns of Cu<sub>x</sub>S<sub>y</sub> nanoparticles prepared in (a) OLA, (b) HDA, and (c) DDA at 230 °C using (I) complex 1 and (II) complex 2.

An increase in the reaction temperature resulted in an improvement in the quality and crystallinity of the copper sulphide NPs, and various shapes were formed (Figure 6). When OLA was used as a capping agent, a mixture of rectangular and truncated triangle-shaped copper sulphide NPs were observed with sizes of approximately 40–120 nm (Figure 6a) using complex 1. The use of HDA resulted in the formation of irregular cubic- and rectangular-shaped particles with estimated sizes of 101–200 nm, and DDA produced irregular cubic NPs with sizes of 61–119 nm (Figure 6b,c). The variations in the morphologies of the copper sulphide NPs were attributed to the influence of the length of the alkyl chains of the capping

agents, which appeared to control the resultant sizes and shapes [44]. When complex 2 was used as a precursor under similar synthetic conditions, agglomerated NPs were formed in OLA while HAD resulted in irregular cubic NPs with sizes of 45–115 nm (Figure 6e). Under the same conditions with DDA, rectangular and cubic NPs with an estimated size of 66–225 nm were formed (Figure 6f). The selected area electron diffraction (SAED) of the nanoparticles from complexes 1 and 2, prepared at 190 °C and 230 °C, confirmed the crystalline nature of the nanoparticles Figures 5g–i, 6g–i, S5a–c and S6a–c). The particle size distributions of  $\text{Cu}_9\text{S}_5$  nanoparticles are presented in Figures 7 and S7c–f.

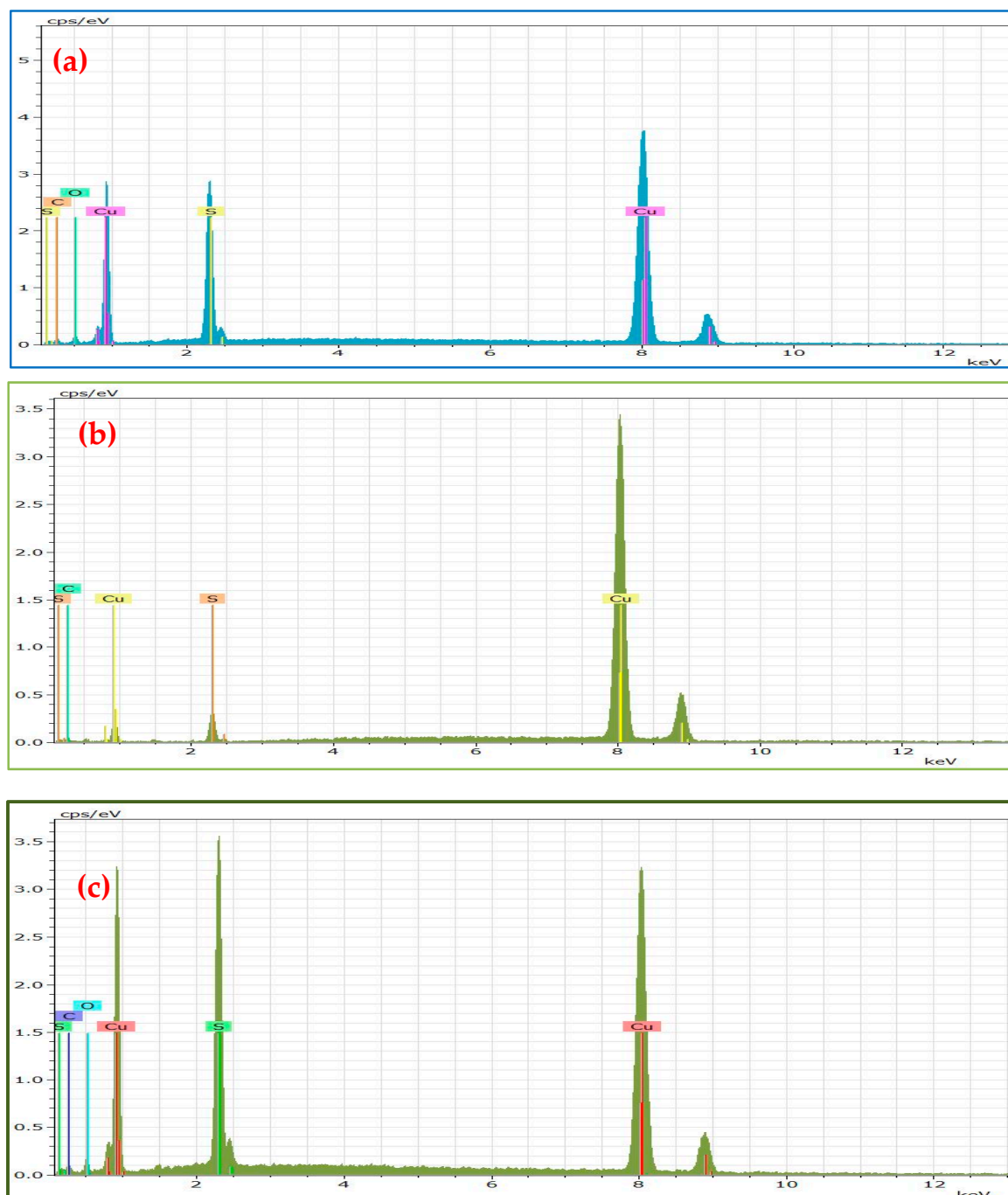


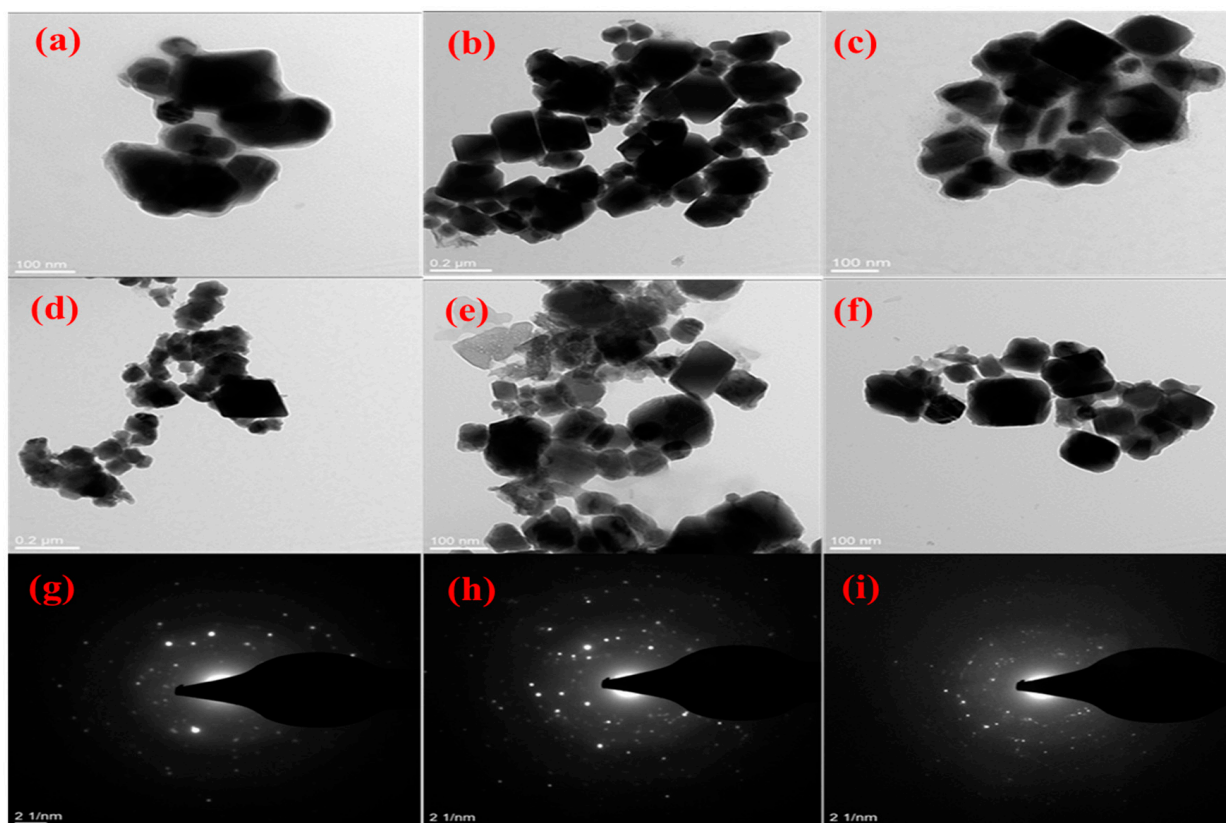
**Figure 4.** EDX spectra of  $\text{Cu}_x\text{S}_y$  nanoparticles prepared in (a) OLA, (b) HDA, and (c) DDA at 190 °C using complex 1.

**Table 1.** EDX analysis of OLA@Cu<sub>9</sub>S<sub>5</sub>, HDA@Cu<sub>9</sub>S<sub>5</sub>, and DDA@Cu<sub>9</sub>S<sub>5</sub> NPs obtained at 190 °C using complex 1 and complex 2.

OLA <sub>1</sub> @Cu <sub>9</sub> S <sub>5</sub>		HDA <sub>1</sub> @Cu <sub>9</sub> S <sub>5</sub>		DDA <sub>1</sub> @Cu <sub>9</sub> S <sub>5</sub>		OLA <sub>2</sub> @Cu <sub>9</sub> S <sub>5</sub>		HDA <sub>2</sub> @Cu <sub>9</sub> S <sub>5</sub>		DDA <sub>2</sub> @Cu <sub>9</sub> S <sub>5</sub>	
Element	Weight %	Element	Weight %	Element	Weight %	Element	Weight %	Element	Weight %	Element	Weight %
Cu	49.50	Cu	61.06	Cu	46.47	Cu	27.77	Cu	31.67	Cu	31.07
S	25.44	S	27	S	25.33	S	13.90	S	18.50	S	17.66
O	4.92	O	/	O	6.61	O	7.90	O	19.52	O	19.22
C	20.14	C	11.94	C	21.5	C	50.43	C	30.31	C	32.05
Cu/S	1.94:1	Cu/S	2.26:1	Cu/S	1.83:1	Cu/S	1.99:1	Cu/S	1.71:1	Cu/S	1.76:1

**Table 2.** EDX analysis of OLA@Cu<sub>9</sub>S<sub>5</sub>, HDA@Cu<sub>9</sub>S<sub>5</sub>, and DDA@Cu<sub>9</sub>S<sub>5</sub> NPs obtained at 230 °C using complex 1 and complex 2.

OLA <sub>1</sub> @Cu <sub>9</sub> S <sub>5</sub>		HDA <sub>1</sub> @Cu <sub>9</sub> S <sub>5</sub>		DDA <sub>1</sub> @Cu <sub>9</sub> S <sub>5</sub>		OLA <sub>2</sub> @Cu <sub>9</sub> S <sub>5</sub>		HDA <sub>2</sub> @Cu <sub>9</sub> S <sub>5</sub>		DDA <sub>2</sub> @Cu <sub>9</sub> S <sub>5</sub>	
Element	Weight %	Element	Weight %	Element	Weight %	Element	Weight %	Element	Weight %	Element	Weight %
Cu	59.86	Cu	60.53	Cu	61.56	Cu	58.81	Cu	59.57	Cu	56.54
S	31.94	S	33.27	S	32.78	S	31.97	S	33.32	S	29.56
O	8.20	O	6.20	O	5.66	O	9.22	O	7.11	O	13.90
C	59.86	C	/	C	/	C	/	C	/	C	/
Cu/S	1.87:1	Cu/S	1.81:1	Cu/S	1.87:1	Cu/S	1.84:1	Cu/S	1.80:1	Cu/S	1.91:1

**Figure 5.** TEM images of Cu<sub>x</sub>S<sub>y</sub> nanoparticles prepared in (a,d) OLA, (b,e) HDA, and (c,f) DDA at 190 °C using complexes 1 and 2; SAED patterns of nanoparticles prepared in (g) OLA, (h) HDA and (i) DDA at 190 °C from complex 1.



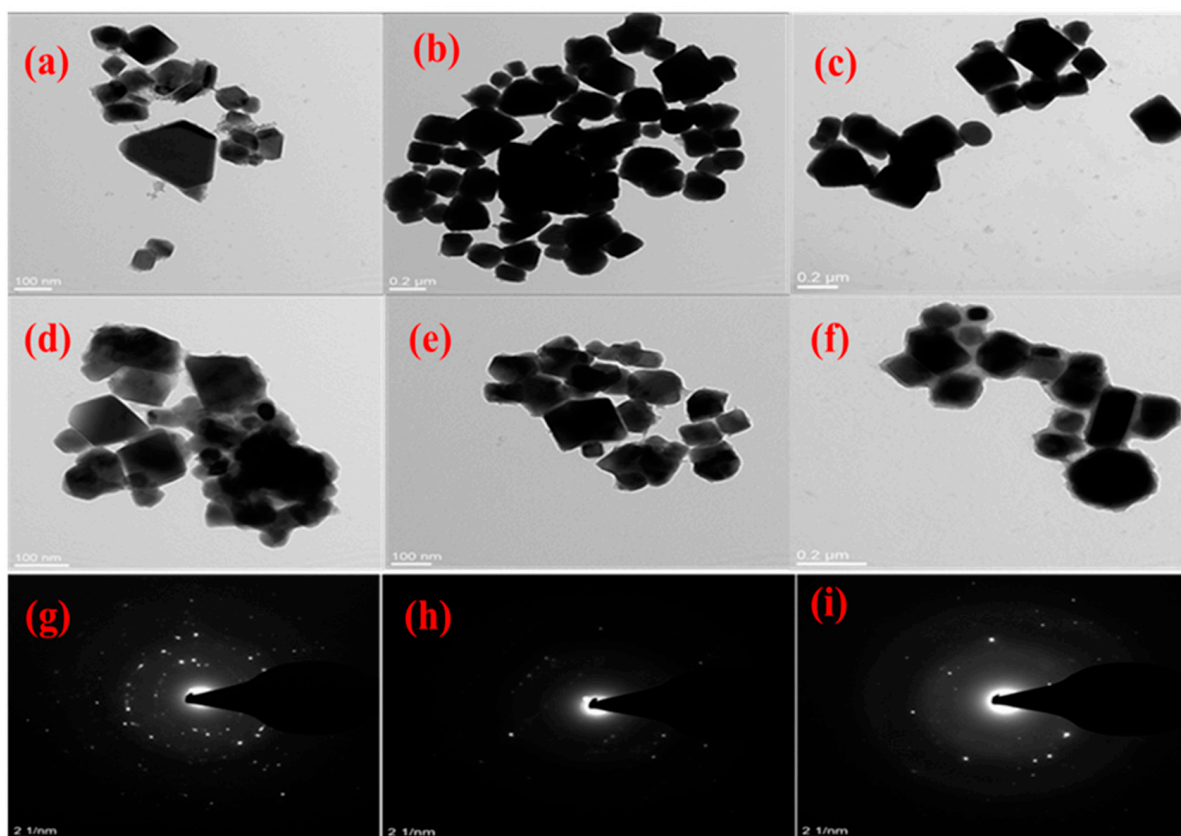


**Figure 6.** TEM images of  $\text{Cu}_x\text{S}_y$  nanoparticles prepared in (a,d) OLA, (b,e) HDA, and (c,f) DDA at 190 °C using complexes 1 and 2; SAED patterns of nanoparticles prepared in (g) OLA, (h) HDA, and (i) DDA at 230 °C from complex 1.

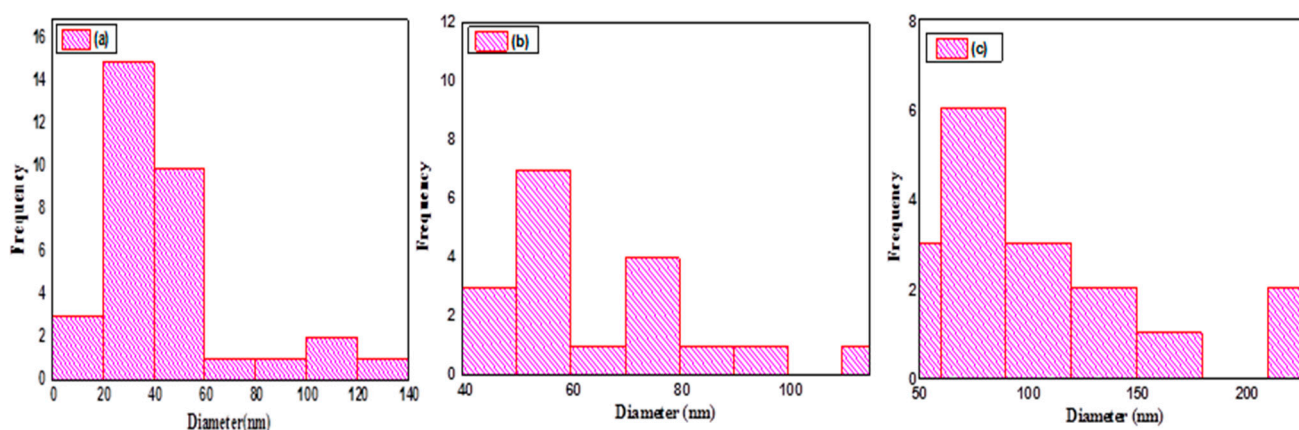


**Figure 7.** Particle size distribution for  $\text{Cu}_x\text{S}_y$  nanoparticles prepared in (a) OLA, (b) HDA, and (c) DDA at 230 °C using complex 2.

The SEM analyses were conducted to investigate the surface morphology of  $\text{Cu}_9\text{S}_5$  nanoparticles using complexes 1 and 2 as precursors, and the results are presented in Figure 8. When complex 1 was thermolysed at 190 °C using OLA, HDA, and DDA as capping agents, agglomerated, granular  $\text{Cu}_9\text{S}_5$  particles were formed (Figure 8a–c). In HDA, a less porous surface was observed (Figure 8b) while a porous surface was observed in DDA (Figure 8c). When complex 2 was used as a precursor, clusters were formed in OLA (Figure 8d), agglomerated seeds in HDA (Figure 8e), and agglomerated, porous, irregularly spherical NPs in DDA (Figure 8f).

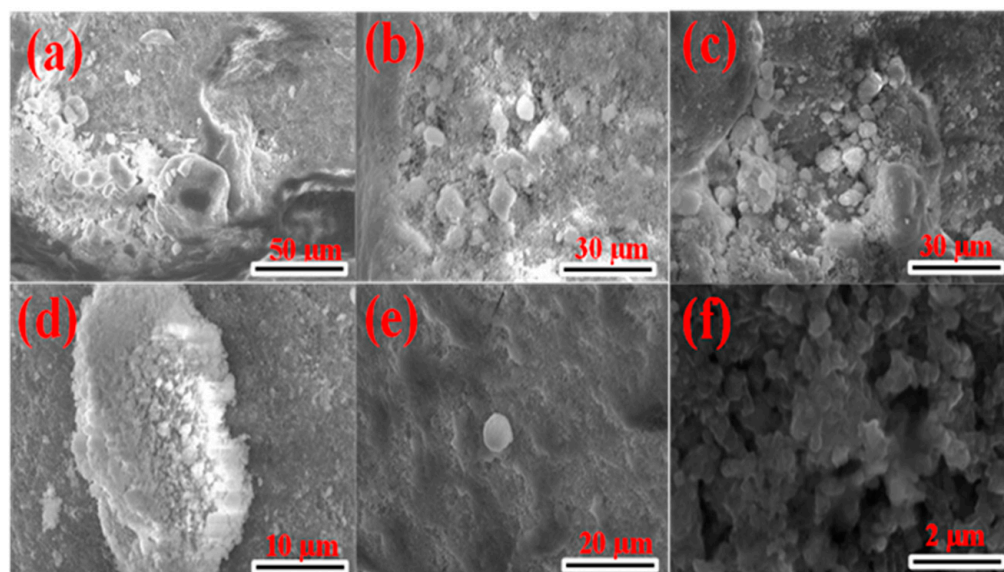


**Figure 8.** SEM images of  $\text{Cu}_x\text{S}_y$  nanoparticles prepared in (a,d) OLA, (b,e) HDA, and (c,f) DDA at  $190^\circ\text{C}$  using the complexes 1 and 2.

The SEM images of the  $\text{Cu}_9\text{S}_5$  nanoparticles obtained at  $230^\circ\text{C}$  are shown in Figure S8. Agglomerated, irregularly spherical particles were formed in OLA (Figure S8a) while rock-shaped particles were formed in both HDA and DDA (Figure S8b,c). A similar trend (i.e., rock-shaped particles) was observed when complex 2 was thermolysed in OLA, HDA, and DDA (Figure S8e,f).

### 2.2.3. Optical Properties of $\text{Cu}_x\text{S}_y$ Nanoparticles

The ultraviolet-visible (UV-Vis) absorption spectra and their corresponding Tauc plots for copper sulphide NPs synthesized in OLA, HDA, and DDA and using complexes 1 and 2 at  $190^\circ\text{C}$  are presented in Figure S9a,b and Figure 9 respectively. All the samples exhibited broad absorption in the visible region (400–650 nm) and extended into the near-infrared region at approximately 800 nm. The energies obtained were within 2.57–2.70 eV range for complex 1 and 2, 2.55–3.00 eV for complex 2. These values correspond to a blue shift as compared  $\text{Cu}_x\text{S}_y$  bulk values (1.2–2.5 eV) due to quantum confinement effect of the  $\text{Cu}_x\text{S}_y$  NPs [45]. The obtained materials showed variations in their optical properties according to the capping agent and precursor used. This difference in energy bandgap was attributed to the stoichiometric variations and the arrangement of the cations and anions in the atomic structures of the compounds [4]. This blue shift was more pronounced in  $\text{OLA@Cu}_x\text{S}_y$  (2.70 eV and 3.00 eV) than in  $\text{HDA@Cu}_x\text{S}_y$  (2.64 eV and 2.58) and  $\text{DDA@Cu}_x\text{S}_y$  (2.57 eV and 2.55) NPs when complexes 1 and 2 were used, respectively, as precursors. This could be due to the differences in the carbon chains of the capping molecules, as OLA is a  $\text{C}_{18}$  branched amine while HDA and DDA are, respectively,  $\text{C}_{16}$  and  $\text{C}_{12}$  linear amines.

The same trend in the optical properties was observed when the reaction temperature was raised to  $230^\circ\text{C}$  with a slight decrease in the absorption-band edges, as compared to  $190^\circ\text{C}$ ; the bandgap energies varied within the range of 2.52–2.76 eV for complex 1 and 2.56–2.83 eV for complex 2. This result was consistent with previous research [4]. The absorption spectra with their corresponding Tauc plots are presented in Figures S10a,b and S11.

### 2.3. Photocatalytic Activity of $\text{Cu}_x\text{S}_y$ Nanoparticles on Methylene-Blue Dye

The photocatalytic activities of  $\text{Cu}_9\text{S}_5$  NPs synthesized at  $190^\circ\text{C}$  and  $230^\circ\text{C}$  were examined using a synthetic effluent containing methylene blue (MB). Figures 10, S12 and S13 display the absorption spectra of the aliquots collected at different time intervals (i.e., at 15, 30, 45, 60, 75, and 90 min) after UV irradiation using a mixed solution of  $\text{Cu}_9\text{S}_5$



NPs and MB. It was observed that as the irradiation time increased, there was a decrease in the absorption peak at 663 nm, which indicated MB degradation. The OLA<sub>1</sub>@Cu<sub>9</sub>S<sub>5</sub>, HDA<sub>1</sub>@Cu<sub>9</sub>S<sub>5</sub>, and DDA<sub>1</sub>@Cu<sub>9</sub>S<sub>5</sub> NPs obtained at 190 °C using complex 1 showed degradation efficiencies of 63.6%, 73.6%, and 80.0%, respectively, after 90 min of UV irradiation (Table 3, Figures 10a and 11a). A slight increase was observed in degradation rates when complex 2 was used as a precursor under the same reaction conditions, which indicated the effect of the precursor type on the NPs' photocatalytic properties. Degradation rates of 76.2%, 76.2%, and 80.0% were obtained for OLA<sub>2</sub>@Cu<sub>9</sub>S<sub>5</sub>, HDA<sub>2</sub>@Cu<sub>9</sub>S<sub>5</sub>, and DDA<sub>2</sub>@Cu<sub>9</sub>S<sub>5</sub> NPs, respectively (Table 3, Figures 10b and 11b).

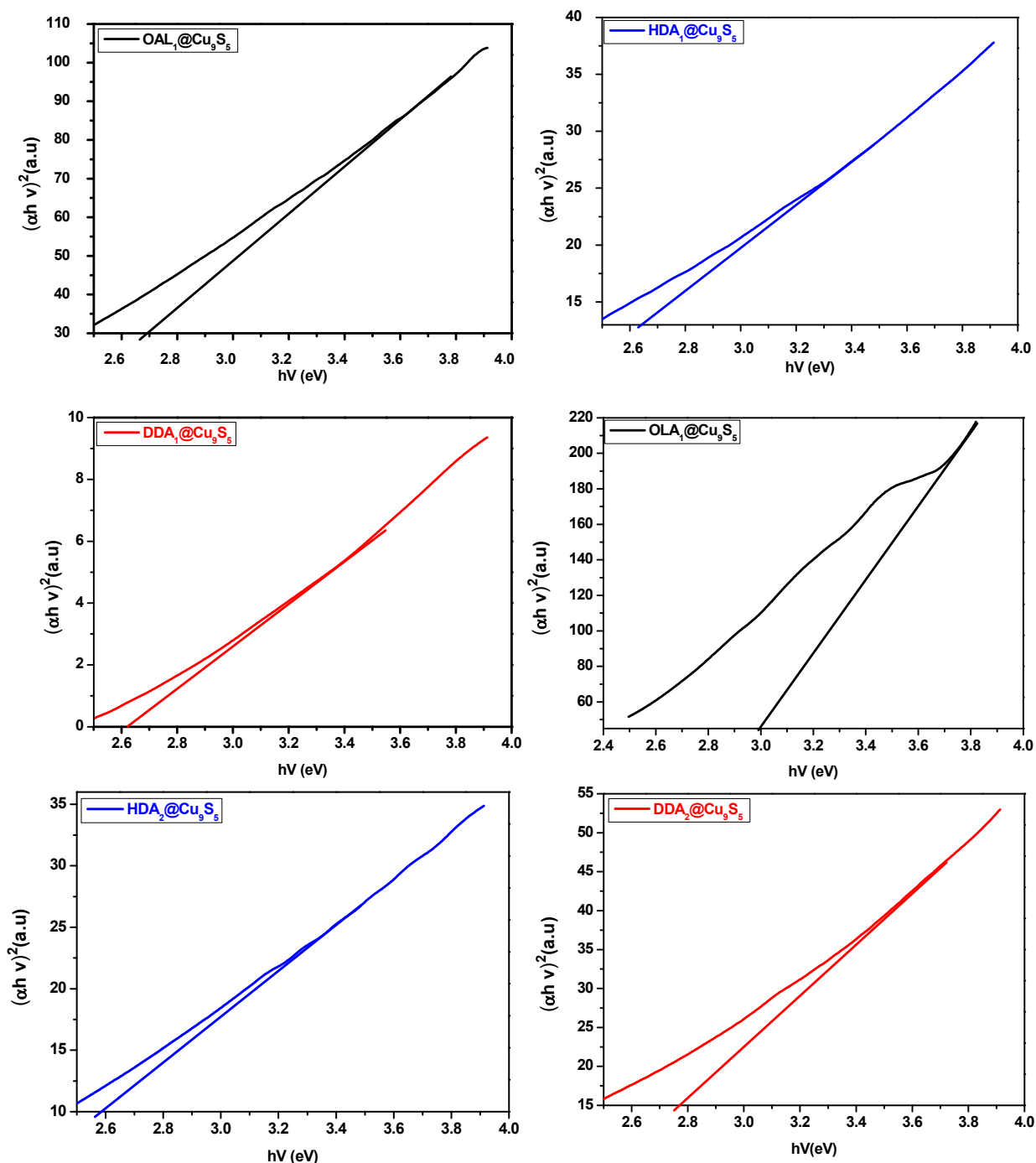


Figure 9. Tauc bandgap graphs of Cu<sub>9</sub>S<sub>5</sub> nanoparticles prepared in OLA, HDA, and DDA at 190 °C while using either complex 1 or 2.

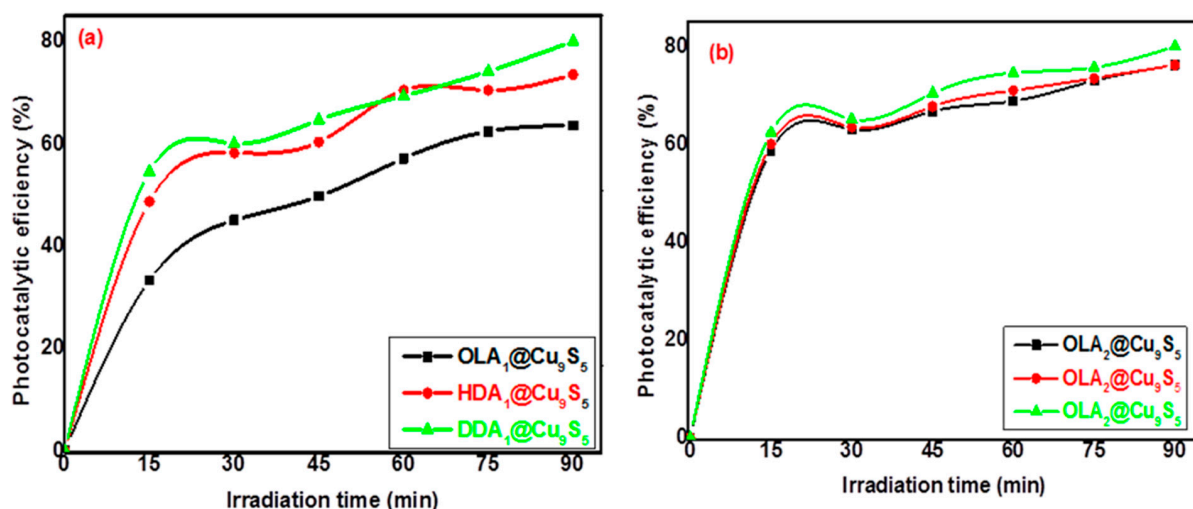


Figure 10. Degradation-efficiency curves of MB at different irradiation times using (a) complex 1 and (b) complex 2 at 190 °C.

Table 3. Degradation efficiencies of OLA@Cu<sub>9</sub>S<sub>5</sub>, HDA@Cu<sub>9</sub>S<sub>5</sub>, and DDA@Cu<sub>9</sub>S<sub>5</sub> NPs obtained at 190 °C using complexes 1 and 2.

	t (min)	15	30	45	60	75	90
OLA <sub>1</sub> @Cu <sub>9</sub> S <sub>5</sub>	η (%)	33.3	46.0	49.7	57.1	62.4	63.6
HDA <sub>1</sub> @Cu <sub>9</sub> S <sub>5</sub>	η (%)	48.7	58.2	60.3	70.4	70.4	73.6
DDA <sub>1</sub> @Cu <sub>9</sub> S <sub>5</sub>	η (%)	54.6	60.0	64.6	69.3	74.1	80.0
OLA <sub>2</sub> @Cu <sub>9</sub> S <sub>5</sub>	η (%)	58.7	60.0	66.7	68.8	73.0	76.2
HDA <sub>2</sub> @Cu <sub>9</sub> S <sub>5</sub>	η (%)	60.0	63.5	67.7	71.0	73.5	76.2
DDA <sub>2</sub> @Cu <sub>9</sub> S <sub>5</sub>	η (%)	62.4	65.1	70.4	74.6	75.7	80.0

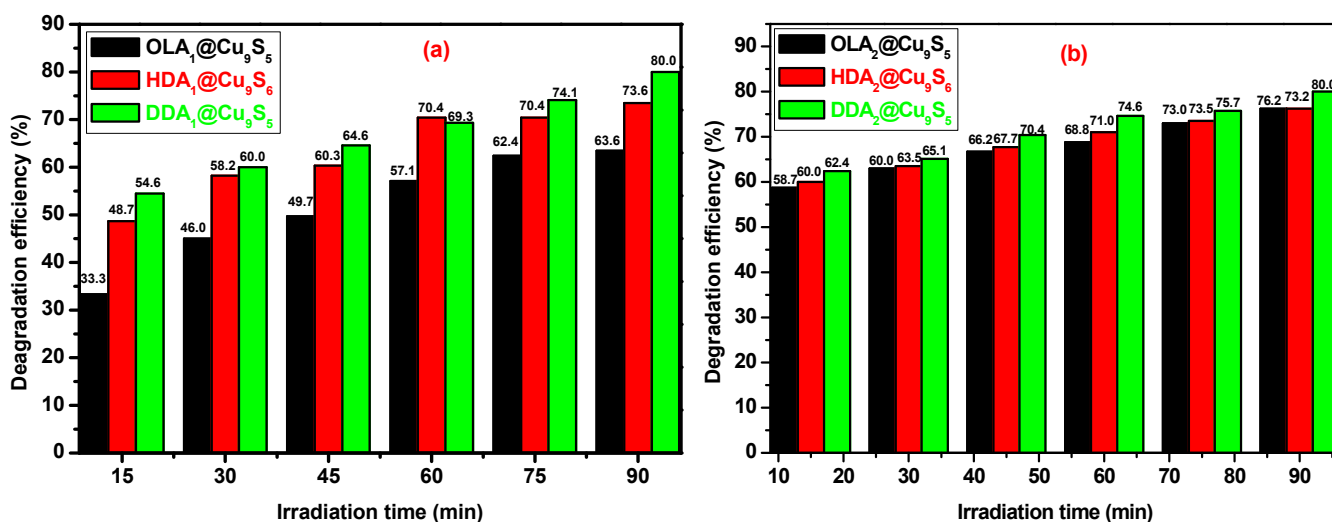
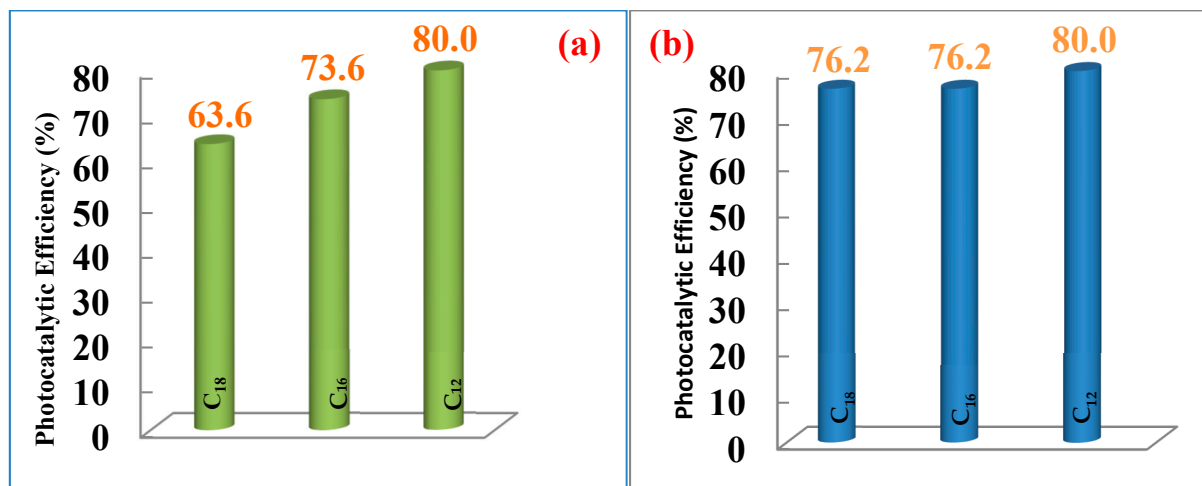


Figure 11. Histograms of degradation efficiencies of MB at different irradiation times using (a) complex 1 and (b) complex 2 at 190 °C.

The results also showed an increase in the degradation rates for MB with a decrease in the length of the carbon chain of the capping agent used (Figure 12). The Cu<sub>9</sub>S<sub>5</sub> NPs produced from DDA (C<sub>12</sub>) exhibited higher photocatalytic activity, as compared to copper sulphide NPs obtained with HDA (C<sub>16</sub>) and OLA (C<sub>18</sub>). This may have been related to the steric properties of the ligand, which may have affected its surface coverage of the Cu<sub>9</sub>S<sub>5</sub> NPs. The enhancement of photocatalytic activities may have been due to the narrowing

of the bandgap as well as the reduction in the electron–hole pair recombination and the porous surface [46]. The results obtained showed improved photocatalytic activities in copper sulphide NPs with higher degradation rates, compared to those reported by Ajibade et al. [47].



**Figure 12.** Histograms of degradation efficiencies of MB using copper sulphide nanoparticles at 190 °C versus carbon chain of capping agents using (a) complex 1 and (b) complex 2.

An increase in the reaction temperature from 190 °C to 230 °C resulted in a decrease in the photocatalytic properties of the copper sulphide NPs (Table 4 and Figure 13). When complex 1 was used as a precursor, degradation rates of 57.7%, 53.4%, and 54.5% were obtained for the OLA<sub>1</sub>@Cu<sub>9</sub>S<sub>5</sub>, HDA<sub>1</sub>@Cu<sub>9</sub>S<sub>5</sub>, and DDA<sub>1</sub>@Cu<sub>9</sub>S<sub>5</sub> NPs, respectively. A similar trend was observed for complex 2 when the reaction temperature was increased from 190 °C to 230 °C, yielding degradation rates of 47.6%, 47.1%, and 56.1% for the OLA<sub>2</sub>@Cu<sub>9</sub>S<sub>5</sub>, HDA<sub>2</sub>@Cu<sub>9</sub>S<sub>5</sub>, and DDA<sub>2</sub>@Cu<sub>9</sub>S<sub>5</sub> NPs, respectively, which were slightly lower than values obtained for Complex 1 at same temperature.

**Table 4.** Degradation efficiencies of OLA@Cu<sub>9</sub>S<sub>5</sub>, HDA@Cu<sub>9</sub>S<sub>5</sub>, and DDA@Cu<sub>9</sub>S<sub>5</sub> NPs obtained at 230 °C using complexes 1 and 2.

	t (min)	15	30	45	60	75	90
OLA <sub>1</sub> @Cu <sub>9</sub> S <sub>5</sub>	η (%)	45.0	46.6	47.6	49.7	53.4	57.7
HDA <sub>1</sub> @Cu <sub>9</sub> S <sub>5</sub>	η (%)	43.4	46.0	47.1	49.7	51.3	53.4
DDA <sub>1</sub> @Cu <sub>9</sub> S <sub>5</sub>	η (%)	45.5	48.1	49.5	50.8	53.4	54.5
OLA <sub>2</sub> @Cu <sub>9</sub> S <sub>5</sub>	η (%)	40.2	41.2	45.5	47.6	47.6	47.6
HDA <sub>2</sub> @Cu <sub>9</sub> S <sub>5</sub>	η (%)	30.0	30.1	33.3	35.4	41.2	47.1
DDA <sub>2</sub> @Cu <sub>9</sub> S <sub>5</sub>	η (%)	31.2	34.4	39.7	45.0	49.7	56.1

The photocatalytic efficiency of the Cu<sub>9</sub>S<sub>5</sub> NPs on the photodegradation of MB was associated with their sufficient bandgap energy and their efficient production of electron–hole pairs under UV irradiation. It has been reported that the oxidative potential of a material may be reduced with a decrease in the bandgap energy, and this may impact the photocatalytic efficiency of the material [48]. Figure 14 attempts to describe the mechanism of the photocatalytic process, starting from the creation of electron-hole pairs as Cu<sub>9</sub>S<sub>5</sub> nanoparticles receive UV irradiation. The excited electrons create O<sub>2</sub><sup>•−</sup> radicals from dissolved oxygen while electron-hole participate in the oxidation of surface-adsorbed water to form hydroxyl radicals (HO<sup>•</sup>) which react with the dye molecule [48]. The degradation efficiencies of OLA<sub>1</sub>@Cu<sub>9</sub>S<sub>5</sub>, HDA<sub>1</sub>@Cu<sub>9</sub>S<sub>5</sub>, and DDA<sub>1</sub>@Cu<sub>9</sub>S<sub>5</sub> NPs obtained at 190 °C suggested that copper sulphide nanoparticles could be exploited as potential and effective

photocatalysts for the removal of organic pollutants from water effluents. A summary of the results obtained is presented in Table 5.

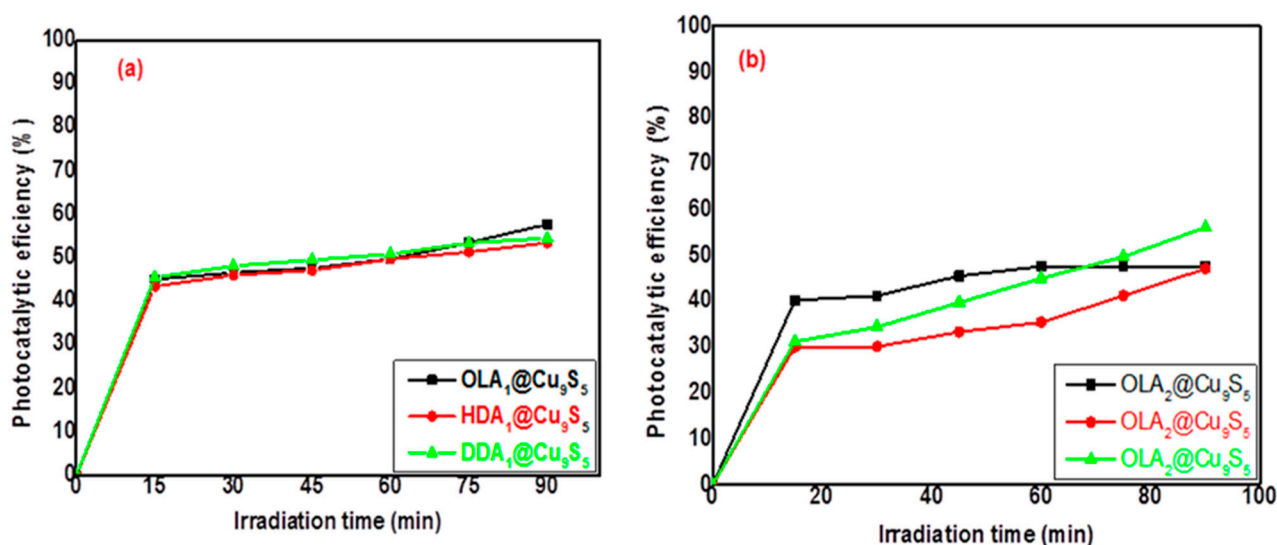


Figure 13. Degradation efficiency curves of MB at different irradiation times using (a) complex 1 and (b) complex 2 as precursors at 230 °C.

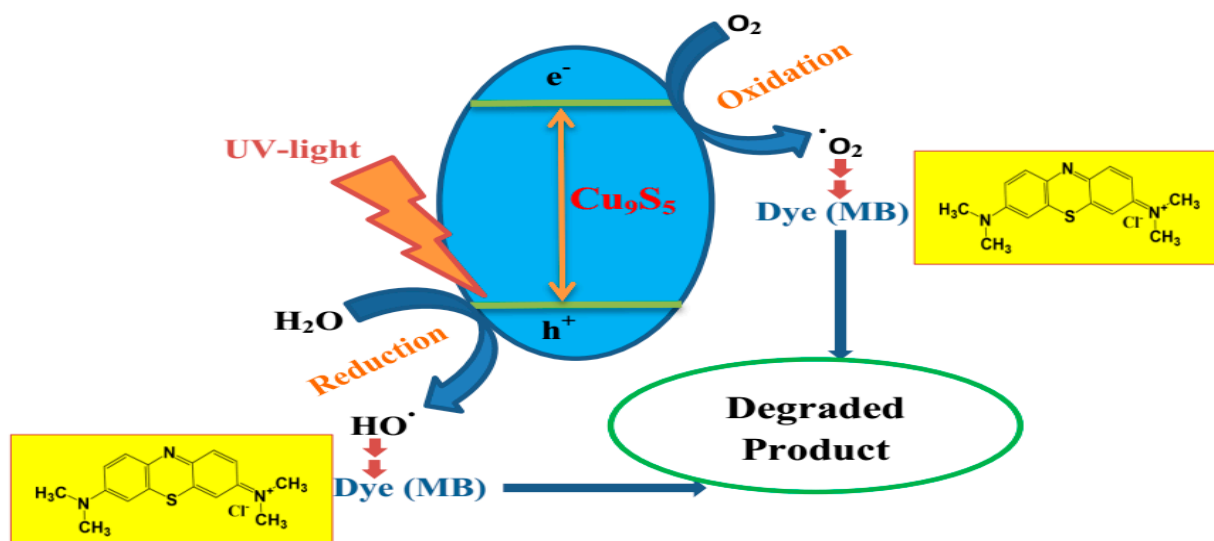


Figure 14. Mechanism of MB degradation by Cu<sub>x</sub>S<sub>y</sub> NPs under UV irradiation.

**Table 5.** Summary of the reaction conditions, sizes, shapes optical, and photocatalytic properties of copper sulphide NPs.

Complexes	Capping Agent	Reaction Temp (°C)	Energy Bandgap (eV)	Phase (Formula)	Morphology	Average Size (nm)	Degradation Rates (%) after 90 min
1	OLA	190	2.70	Mixture of Cu <sub>9</sub> S <sub>5</sub> & Cu <sub>7</sub> S <sub>5</sub>	Agglomerated Irregular	49–80	63.6
	HDA	190	2.64	Cu <sub>9</sub> S <sub>5</sub>	Rectangular and cubic	46–134	73.6
	DDA	190	2.57	Cu <sub>9</sub> S <sub>5</sub>	Rectangular and irregular	53–154	80.0
	OLA	230	2.60	Cu <sub>9</sub> S <sub>5</sub>	Rectangular and truncated	40–120	57.7
	HDA	230	2.76	Cu <sub>9</sub> S <sub>5</sub>	Irregular cubic and rectangular	101–200	53.4
	DDA	230	2.64	Cu <sub>9</sub> S <sub>5</sub>	Irregular cubic	61–119	54.5
2	OLA	190	3.00	Cu <sub>9</sub> S <sub>5</sub>	Agglomerated	32–75	76.2
	HDA	190	2.58	Cu <sub>9</sub> S <sub>5</sub>	Semi-spherical and rectangular	43–125	76.2
	DDA	190	2.55	Cu <sub>9</sub> S <sub>5</sub>	Irregular cubic	49–196	80.0
	OLA	230	2.83	Cu <sub>9</sub> S <sub>5</sub>	Agglomerated	34–128	47.6
	HDA	230	2.76	Cu <sub>9</sub> S <sub>5</sub>	Irregular cubic	45–115	47.1
	DDA	230	2.73	Cu <sub>9</sub> S <sub>5</sub>	Rectangular and cubic	66–225	56.1

### 3. Materials and Methods Experimental

#### 3.1. Chemicals

Hexadecylamine (HDA, 90%), dodecylamine (DDA, 90%), oleylamine (OLA, 70%), 2-thiophenecarboxaldehyde (99%), 2-acethylthiophene (99%), thiosemicarbazide (99%), copper chloride dihydrate (98%), ethanol (99.5%), methanol (99.5%), toluene (99.5%), and acetone (99.5%) were obtained from a commercial source and used without any further purification.

#### 3.2. Instrumentation

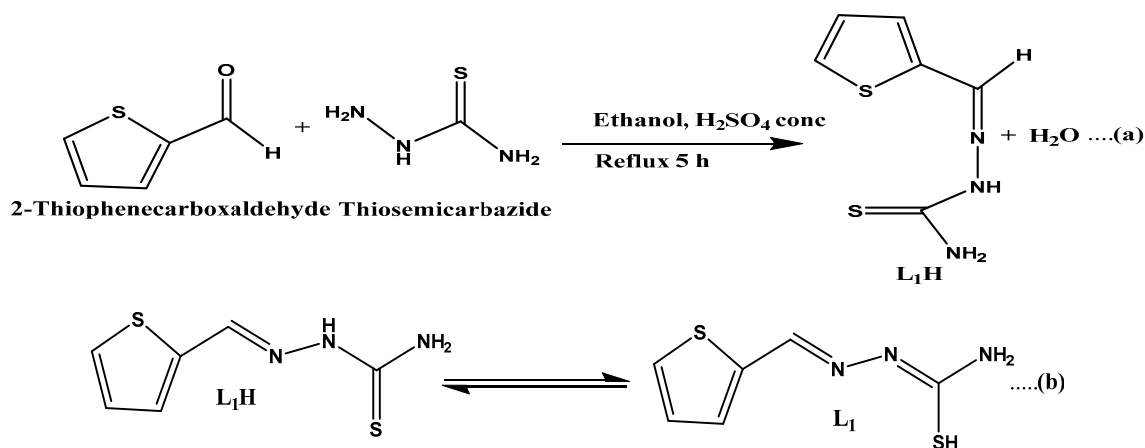
Melting points were determined using an SMP11 melting-point-measurement instrument. Microanalysis (C, H, and N) data were obtained from a Perkin Elmer automated model 2400 series II CHNS/O analyser. Fourier-transform infrared (FTIR) spectra were recorded on an FTIR Perkin Elmer 400 spectrometer from 4000 cm<sup>-1</sup> to 450 cm<sup>-1</sup>. Thermal analyses were conducted using a Perkin Elmer Pyris 6 TGA device up to 600 °C. X-ray diffraction (XRD) measurements were performed using X'Pert MPD diffractometer with Cu K $\alpha$  radiation ( $\lambda = 1.5406 \text{ \AA}$ ). TEM analyses were performed using a CM200-FEI at 200 KV. Scanning electron microscopy (SEM) analyses were performed using a Quanta 650 FEG-FEI. Elemental compositions of Cu<sub>x</sub>S<sub>y</sub> were obtained using an energy-dispersive X-ray (EDX). Optical absorption measurements were conducted using an Ocean Insight FX-VIS-IRS-ES spectrophotometer at room temperature.

#### 3.3. Preparation of Thiosemicarbazone Ligands

Thiosemicarbazone ligands were prepared using a method described in the literature, with slight modification [32,33].

### 3.3.1. Synthesis of 2-Thiophenecarboxaldehyde Thiosemicarbazone ( $L_1H$ ) Ligand

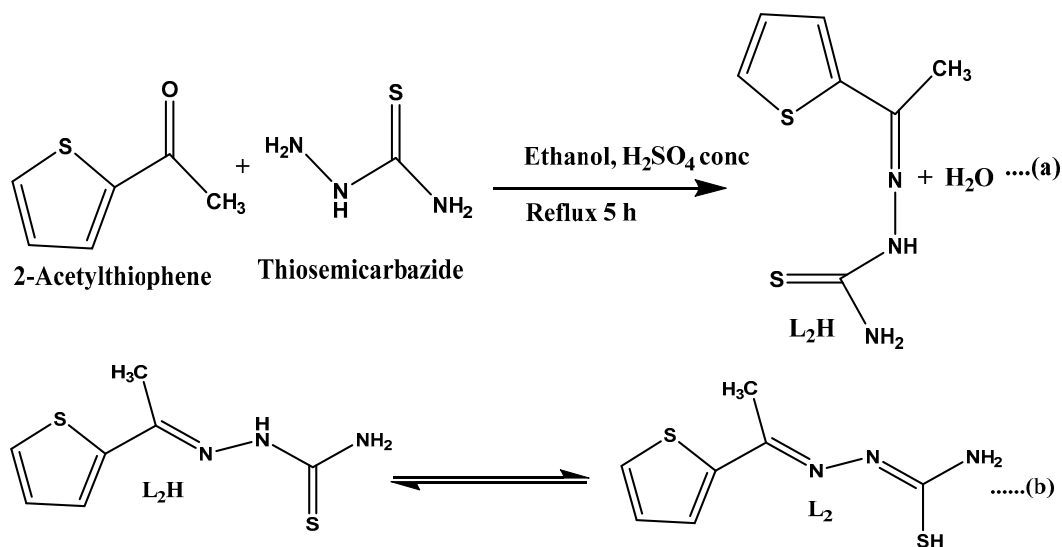
A mass of 0.38 g (3 mmol) of 2-thiophenecarboxaldehyde was dissolved in 15 mL of hot ethanol and then added dropwise into a solution containing 0.33 g (3 mmol) of thiosemicarbazide dissolved in 25 mL hot ethanol in a round-bottom flask. The reaction mixture was then stirred continuously, and 2–3 drops of concentrated  $H_2SO_4$  were added. The resulting mixture was heated under reflux at  $80\text{ }^\circ\text{C}$  for 5 h. The yellow precipitate obtained was filtered, washed with ethanol, and then dried in air. The reaction equation is represented in Scheme 1. Yield: 69%. Melting point:  $182 \pm 2\text{ }^\circ\text{C}$ . Anal. Calc. for ( $C_6H_7N_3S_2$ ): C, 38.69; H, 4.33; N, 22.56. Found: C, 38.90; H, 3.81; N, 22.68. Significant Infrared (IR) bands: ( $\text{cm}^{-1}$ ):  $\nu(\text{NH}_2)$ : 3361,  $\nu(\text{N-H})$ : 3125,  $\nu(\text{C=N})$ : 1582,  $\nu(\text{N-N})$ : 1044,  $\nu(\text{C=S})$ : 835.



**Scheme 1.** Equation of synthesis of the ligand, 2-thiophenecarboxaldehyde thiosemicarbazone ( $L_1H$ ) (a) and resonance forms also shown in (b).

### 3.3.2. Synthesis of 2-Acetylthiophene Thiosemicarbazone ( $L_2H$ ) Ligand

The same reaction procedure as described above was used for the synthesis of  $L_2H$  using a mass of 0.34 g (3 mmol) of 2-acetylthiophene. The light-yellow precipitate obtained was filtered, washed with ethanol, and then dried in air. The reaction equation is represented in Scheme 2. Yield: 95.4%. Melting point:  $146 \pm 2\text{ }^\circ\text{C}$ . Anal. Calc. for ( $C_7H_9N_3S_2$ ): C, 41.97; H, 5.03; N, 20.58. Found: C, 40.82; H, 4.79; N, 20.17. Significant IR bands: ( $\text{cm}^{-1}$ ):  $\nu(\text{NH}_2)$ : 3409,  $\nu(\text{N-H})$ : 3157,  $\nu(\text{C=N})$ : 1594,  $\nu(\text{N-N})$ : 1040,  $\nu(\text{C=S})$ : 830.

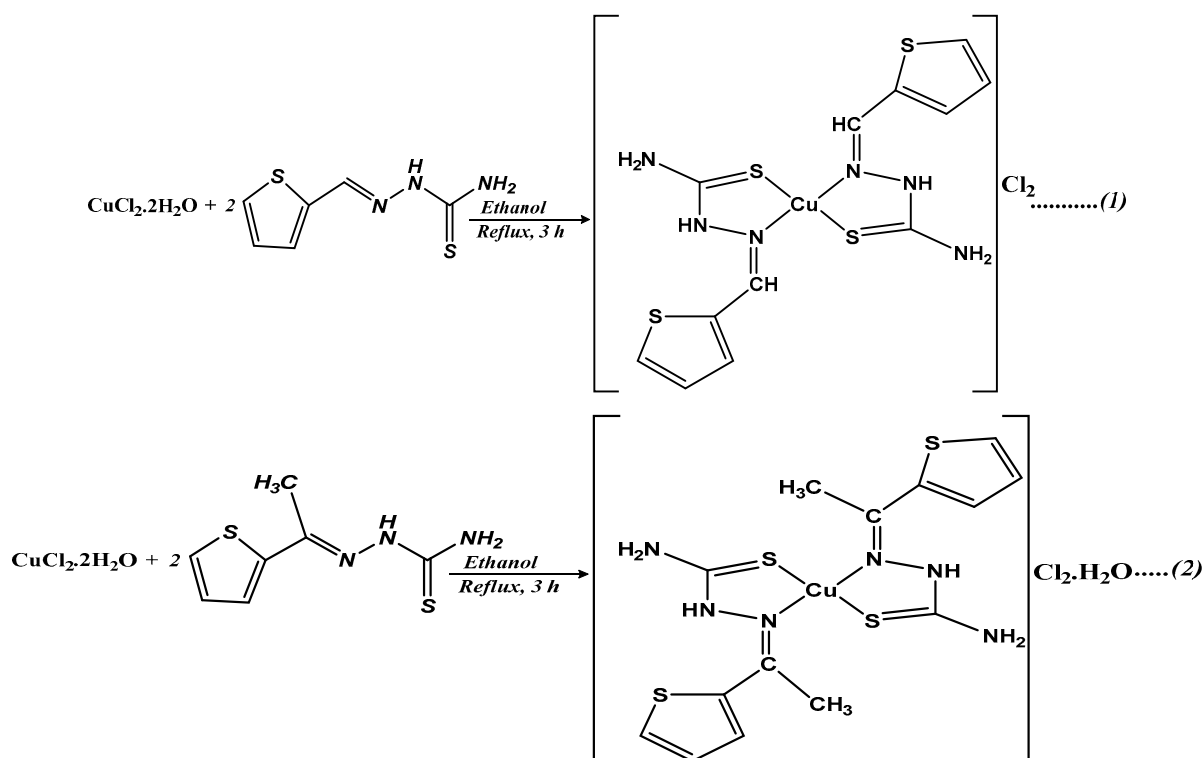


**Scheme 2.** Equation of synthesis of the ligand, 2-acetylthiophene thiosemicarbazone ( $L_2H$ ) (a) and resonance forms also shown in (b).



### 3.4. Preparation of Cu(II) Complexes (Complex 1 and 2)

A hot ethanolic solution (20 mL) of 2-(thiophen-2-ylmethylene)hydrazine-1-carbothioamide ligand ( $L_1H$ ) (1.10 g, 6 mmol) was added dropwise to a hot ethanolic solution (20 mL) of  $CuCl_2 \cdot 2H_2O$  (0.52 g, 3 mmol). The mixture was stirred and heated under reflux for 3 h at 80 °C (Scheme 3). The precipitate obtained was allowed to cool at room temperature and then separated by filtration, washed with ethanol, and then dried at room temperature to obtain complex 1 as a pale-yellow powder. Yield: 71.3%. Melting point > 300 °C. Anal. Calc. for  $[Cu(C_6H_8N_3S_2)_2]Cl_2$ : C, 28.54; H, 2.79; N, 16.64. Found: C, 28.77; H, 2.86; N, 16.84. Significant IR bands ( $cm^{-1}$ ):  $\nu(NH_2)$ : 3422–3235,  $\nu(C=N)$ : 1608,  $\nu(N-N)$ : 1034,  $\nu(C=S)$ : 831,  $\nu(M-N)$ : 555.



**Scheme 3.** Equation for the synthesis of (1) complex 1 and (2) complex 2.

The same method was used for the synthesis of complex 2 using the ligand 2-(1-(thiophen-2-yl) ethylidene)hydrazine-1-carbothioamide ( $L_2H$ ) (1.20 g, 6 mmol) (Scheme 3). Complex 2 was obtained as a pale-yellow powder. Yield: 59%. Melting point > 300 °C. Anal. Calc. for  $[Cu(C_7H_{10}N_3S_2)_2]Cl_2 \cdot H_2O$ : C, 30.51; H, 3.66; N 15.25. Found: C, 29.87; H, 3.29; N, 15.25. Significant IR bands( $cm^{-1}$ ):  $\nu(NH_2)$ : 3415–3254,  $\nu(C=N)$ : 1602,  $\nu(N-N)$ : 1109,  $\nu(C=S)$ : 820, (M-N): 513.

### 3.5. Preparation of Copper Sulphide Nanoparticles

In a typical synthetic method employing hot-injection thermolysis, 3.0 mL of oleylamine (OLA) was placed in a three-necked flask and purged with  $N_2$ . The capping agent was slowly heated to the desired temperature (i.e., 190 °C or 230 °C), and a mass 200 mg of complex 1 dissolved in 3.0 mL of OLA was injected into the heated OLA in a three-necked flask at 190 °C while stirring. A decrease in temperature of approximately 20 °C was observed, and the solution turned brown in colour. The reaction temperature was maintained at 190 °C, and after 30 min of stirring, heating was stopped, and methanol was added to flocculate the copper sulphide NPs [8,9]. The precipitate was separated by centrifugation and then dispersed in toluene to obtain dark-brownish OLA-capped  $Cu_xS_y$  nanoparticles (OLA@ $Cu_xS_y$ ).

The above reaction procedure was repeated at a reaction temperature of 230 °C, varying the capping groups from hexadecylamine (HDA) to dodecylamine (DDA) and replacing the precursor with complex 2 in Scheme 3.

### 3.6. Photocatalytic Studies

The photocatalytic activities of OLA-, HDA-, and DDA-capped Cu<sub>9</sub>S<sub>5</sub> NPs were evaluated by degrading methylene blue (MB) as a test contaminant in an aqueous solution under ultraviolet (UV)-light irradiation value of 60 W/m<sup>2</sup>. A 5 mg of MB solution was prepared in a 500 mL volumetric flask using distilled water (10 ppm). A total of 10 mg of the catalyst was dispersed in 50 mL of aqueous MB solution in a Pyrex beaker. Prior to irradiation, the solution was stirred magnetically in the dark for 15 min to attain adsorption–desorption equilibrium. The resulting solution was then exposed to ultraviolet (UV)-light irradiation ( $\lambda = 368$  nm) for 90 min. Aliquots were collected at 15 min interval and centrifuged to obtain the resulting solution for absorption analysis. The photodegradation efficiency ( $\eta$ ) was calculated using Equation (1) [49].

$$\eta = \frac{A_0 - A_t}{A_0} \times 100 \quad (1)$$

where  $\eta$  is the photodegradation efficiency,  $A_0$  and  $A_t$  are the absorbance values, respectively, before and after 15, 30, 45, 60, 75, and 90 min of illumination and recorded at the maximum absorbance wavelength for MB ( $\lambda = 663$  nm) using a UV-Vis-NIR spectrophotometer.

## 4. Conclusions

Heterocyclic copper(II) thiosemicarbazone complexes were successfully used as single-source precursors for the synthesis of copper sulphide nanoparticles via hot-injection method at 190 °C and 230 °C while using OLA, HDA, and DDA as capping agents. The effects of quantum confinement observed in the energy bandgap of the synthesized copper sulphide NPs were solvent, temperature, and precursor-type dependant. The OLA-capped copper sulphide NPs had a higher energy bandgap of 3.06 eV at 190 °C. The same trend was observed in the formation of various morphologies of copper sulphide nanoparticles, which were influenced by the reaction temperature. Crystalline copper sulphide NPs reported here demonstrates t better photocatalytic properties of these system compared to those reported in recent studies. The degradation rates of MB under UV irradiation were affected by the length of the carbon chain of the primary amine-capping molecule and the type of precursor, and a maximum of 80% was achieved. This study confirmed the potential of synthesized copper sulphide nanophotocatalysts in the treatment of water that has been contaminated with organic pollutants.

**Supplementary Materials:** The following are available online at <https://www.mdpi.com/article/10.3390/catal12010061/s1>, Figure S1: Infrared spectra of ligands and their corresponding complexes. Figure S2: EDX spectra of Cu<sub>x</sub>S<sub>y</sub> nanoparticles prepared in (a) OLA, (b) HDA and (c) DDA at 190 °C using complex 2. Figure S3: EDX spectra of Cu<sub>x</sub>S<sub>y</sub> nanoparticles prepared in (a) OLA, (b) HDA, and (c) DDA at 230 °C using complex 1. Figure S4: EDX spectra of Cu<sub>x</sub>S<sub>y</sub> nanoparticles prepared in (a) OLA, (b) HDA, and (c) DDA at 230 °C using complex 2. Figure S5: SAED patterns of Cu<sub>x</sub>S<sub>y</sub> nanoparticles prepared at 190 °C in (a,c) HDA and (b,d) DDA using complex 1 and complex 2. Figure S6: SAED patterns of Cu<sub>x</sub>S<sub>y</sub> nanoparticles prepared at 230 °C in (a,c) HDA and (b,d) DDA using complex 1 and complex 2. Figure S7: Distribution size of Cu<sub>x</sub>S<sub>y</sub> nanoparticles prepared in (a) OLA, (b) HDA and (c) DDA using complexes 1 at 190 °C. Figure S8: SEM images of Cu<sub>x</sub>S<sub>y</sub> nanoparticles prepared in (a, d) OLA, (b,e) HDA, and (c,f) DDA at 230 °C using the complexes 1 and 2 as precursors. Figure S9: UV-visible-NIR of Cu<sub>x</sub>S<sub>y</sub> nanoparticles prepared in OLA, HDA, and DDA at 190 °C using (a) complex 1 and (b) complex 2 as single-source precursors. Figure S10: UV-visible NIR of Cu<sub>x</sub>S<sub>y</sub> nanoparticles prepared in OLA, HDA, and DDA at 230 °C using (a) complex 1 and (b) complex 2 as single source precursors. Figure S11: Tauc plots of Cu<sub>x</sub>S<sub>y</sub> nanoparticles prepared in OLA, HDA, and DDA at 230 °C using complexes 1 and 2. Figure S12: UV-Vis absorption spectra for methylene blue

photodegradation using  $\text{Cu}_x\text{S}_y$  nanoparticles synthesized at 190 °C. Figure S13: UV-Vis absorption spectra for methylene blue photodegradation using  $\text{Cu}_x\text{S}_y$  nanoparticles synthesized at 230 °C.

**Author Contributions:** Conceptualization, L.D.N., F.C. and P.T.N.; methodology, A.P.Y.; formal analysis, T.G., S.F. and K.I.Y.K.; data curation, A.P.Y.; writing—original draft preparation, A.P.Y., T.G. and K.I.Y.K.; writing—review and editing, L.D.N., S.F., F.C. and P.T.N.; funding acquisition, L.D.N., F.C. and P.T.N.; project management, P.T.N. All authors have read and agreed to the published version of the manuscript.

**Funding:** This research received financial assistance from the Royal Society–DFID capacity building initiative (Grant N°AQ140001) (PTN) and the OWSD for the OWSD Early Career fellowship (UNESCO and the International Development Research Centre, Ottawa, Canada) (LDN). The views expressed herein do not necessarily represent those of UNESCO, IDRC, or the Board of Governors.

**Data Availability Statement:** Data are contained within the article and the Supplementary Materials section.

**Acknowledgments:** The authors are grateful for the mobility bursary (A.P.Y.), which was provided by the University of Lorraine through the Institute Jean Lamour (IJL). The authors would also like to thank the Department of Chemistry of the University of Zululand for TGA and microanalyses.

**Conflicts of Interest:** The authors declare no conflict of interest.

## References

1. Onwudiwe, D.C. Microwave-assisted synthesis of PbS nanostructures. *Heliyon* **2019**, *5*, e01413. [[CrossRef](#)] [[PubMed](#)]
2. Jiade, P.A.A.; Nqombolo, A. Synthesis and structural studies of nickel sulphide and palladium sulphide nanocrystals. *Chalcogenide Lett.* **2016**, *13*, 427–434.
3. Chakraborty, P.; Adhikary, J.; Chatterjee, S.; Biswas, B.; Chattopadhyay, T. Facile syntheses of copper sulfide nanoparticles: Antibacterial and antifungal activity study. *Rasayan J. Chem.* **2016**, *9*, 77–83.
4. Olatunde, O.C.; Onwudiwe, D.C. Temperature Controlled Evolution of Pure Phase  $\text{Cu}_9\text{S}_5$  Nanoparticles by Solvothermal Process. *Front. Mater.* **2021**, *8*, 211. [[CrossRef](#)]
5. Lei, H.; Qin, P.; Ke, W.; Guo, Y.; Dai, X.; Chen, Z. Performance enhancement of polymer solar cells with high work function CuS modified ITO as anodes. *Org. Electron.* **2015**, *22*, 173–179. [[CrossRef](#)]
6. Srinivas, B.; Kumar, B.G.; Muralidharan, K. Stabilizer free copper sulphide nanostructures for rapid photocatalytic decomposition of rhodamine B. *J. Mol. Catal. A Chem.* **2015**, *410*, 8–18. [[CrossRef](#)]
7. Zhang, K.; Khan, M.W.; Zuo, X.; Yang, Q.; Tang, H.; Wu, M. Controllable Synthesis and Photoelectric Properties of Interconnected and Self-Assembled Nanocomposite of Porous Hollow  $\text{Cu}_7\text{S}_4/\text{CuS}$  and Nitrogen-Doped Graphene Oxide. *Electrochim. Acta* **2019**, *307*, 64–75. [[CrossRef](#)]
8. Khan, M.D.; Akhtar, M.; Malik, M.A.; Revaprasadu, N.; O'Brien, P. New examples of phase control in the preparation of copper sulfide nanoparticles and deposition of thin films by AACVD from bis (piperidinedithiocarbamate) copper(II) complex. *ChemistrySelect* **2018**, *3*, 2943–2950. [[CrossRef](#)]
9. Ketchemen, K.I.Y.; Khan, M.D.; Mlowe, S.; Nyamen, L.D.; Ndifon, P.T.; O'Brien, P.; Revaprasadu, N. Tailoring Shape and Crystallographic Phase of Copper Sulfide Nanostructures Using Novel Thiourea Complexes as Single Source Precursors. *J. Inorg. Organomet. Polym. Mater.* **2019**, *29*, 917–927. [[CrossRef](#)]
10. Hsu, Y.-K.; Chen, Y.-C.; Lin, Y.-G. Synthesis of copper sulfide nanowire arrays for high-performance supercapacitors. *Electrochim. Acta* **2014**, *139*, 401–407. [[CrossRef](#)]
11. Pei, L.Z.; Wang, J.F.; Tao, X.X. Synthesis of CuS and  $\text{Cu}_{1.1}\text{Fe}_{1.1}\text{S}_2$  crystals and their electrochemical properties. *Mater. Charact.* **2011**, *62*, 354–359. [[CrossRef](#)]
12. Ayodhya, D.; Venkatesham, M.; Kumari, A.S.; Reddy, G.B.; Ramakrishna, D.; Veerabhadram, G. Photocatalytic degradation of dye pollutants under solar, visible and UV lights using green synthesised CuS nanoparticles. *J. Exp. Nanosci.* **2016**, *11*, 418–432. [[CrossRef](#)]
13. Senthilkumar, M.; Babu, S.M. Synthesis and characterization of hexagonal faceted copper sulfide ( $\text{Cu}_{1.8}\text{S}$ ) nanodisks. *Mater. Sci. Semicond. Process.* **2015**, *40*, 203–208. [[CrossRef](#)]
14. Ajibade, P.A.; Botha, N.L. Synthesis and structural studies of copper sulfide nanocrystals. *Results Phys.* **2016**, *6*, 581–589. [[CrossRef](#)]
15. Ravele, M.P.; Oyewo, O.A.; Onwudiwe, D.C. Controlled Synthesis of CuS and  $\text{Cu}_9\text{S}_5$  and Their Application in the Photocatalytic Mineralization of Tetracycline. *Catalysts* **2021**, *11*, 899. [[CrossRef](#)]
16. Liao, X.-H.; Chen, N.-Y.; Xu, S.; Yang, S.-B.; Zhu, J.-J. A microwave assisted heating method for the preparation of copper sulfide nanorods. *J. Cryst. Growth* **2003**, *252*, 593–598. [[CrossRef](#)]
17. Li, J.; Zhao, H.; Chen, X.; Jia, H.; Zheng, Z. In situ fabricate  $\text{Cu}_2\text{S}$  thin film with hierarchical petal-like nanostructures. *Mater. Res. Bull.* **2013**, *48*, 2940–2943. [[CrossRef](#)]

18. Cheng, Z.; Wang, S.; Si, D.; Geng, B. Controlled synthesis of copper sulfide 3D nanoarchitectures through a facile hydrothermal route. *J. Alloys Compd.* **2010**, *492*, 44–49. [[CrossRef](#)]
19. Botha, N.L.; Ajibade, P.A. Effect of temperature on crystallite sizes of copper sulfide nanocrystals prepared from copper (II) dithiocarbamate single source precursor. *Mater. Sci. Semicond. Processing* **2016**, *43*, 149–154. [[CrossRef](#)]
20. Shen, S.; Zhang, Y.; Peng, L.; Xu, B.; Du, Y.; Deng, M.; Xu, H.; Wang, Q. Generalized synthesis of metal sulfide nanocrystals from single-source precursors: Size, shape and chemical composition control and their properties. *CrystEngComm* **2011**, *13*, 4572–4579. [[CrossRef](#)]
21. Jen-La Plante, I.; Zeid, T.W.; Yang, P.; Mokari, T. Synthesis of metal sulfide nanomaterials via thermal decomposition of single-source precursors. *J. Mater. Chem.* **2010**, *20*, 6612–6617. [[CrossRef](#)]
22. Paca, A.M.; Ajibade, P.A. Synthesis and structural studies of iron sulphide nanocomposites from iron(III) dithiocarbamate single source precursors. *Mater. Chem. Phys.* **2017**, *202*, 143–150. [[CrossRef](#)]
23. Ma, Y.; Wan, H.; Ye, Y.; Chen, L.; Li, H.; Zhou, H.; Chen, J. In-situ synthesis of size tunable silver sulfide nanoparticles to improve tribological properties of the polytetrafluoroethylene-based nanocomposite lubricating coatings. *Tribol. Int.* **2020**, *148*, 106324. [[CrossRef](#)]
24. Pawar, A.S.; Masikane, S.C.; Mlowe, S.; Garje, S.S.; Akerman, M.P.; Revaprasadu, N. Zinc thiosemicarbazone complexes: Single source precursors for alkylamine capped ZnS nanoparticles. *Inorg. Chim. Acta* **2017**, *463*, 7–13. [[CrossRef](#)]
25. Khan, M.D.; Malik, M.A.; Akhtar, J.; Mlowe, S.; Revaprasadu, N. Phase pure deposition of flower-like thin films by aerosol assisted chemical vapor deposition and solvent mediated structural transformation in copper sulfide nanostructures. *Thin Solid Films* **2017**, *638*, 338–344. [[CrossRef](#)]
26. Du, X.-S.; Yu, Z.-Z.; Dasari, A.; Ma, J.; Meng, Y.-Z.; Mai, Y.-W. Facile synthesis and assembly of Cu<sub>2</sub>S nanodisks to corn coblike nanostructures. *Chem. Mater.* **2006**, *18*, 5156–5158. [[CrossRef](#)]
27. Abdelhady, A.L.; Ramasamy, K.; Malik, M.A.; O'Brien, P.; Haighb, S.J.; Raftery, J. New routes to copper sulfide nanostructures and thin films. *J. Mater. Chem.* **2011**, *21*, 17888–17895. [[CrossRef](#)]
28. Krishna, P.M.; Reddy, N.B.G.; Kottam, N.; Yallur, B.C.; Katreddi, H.R. Design and Synthesis of Metal Complexes of (2E)-2-[(2E)-3-Phenylprop-2-en-1-ylidene]hydrazine carbothioamide and Their Photocatalytic Degradation of Methylene Blue. *Sci. World J.* **2013**, *2013*, 828313. [[CrossRef](#)]
29. Jain, M.; Babar, D.G.; Garje, S.S. Ligand-based stoichiometric tuning in copper sulfide nanostructures and their catalytic ability. *Appl. Nanosci.* **2019**, *9*, 353–367. [[CrossRef](#)]
30. Gaber, A.; Refat, M.S.; Belal, A.A.M.; El-Deen, I.M.; Hassa, N.; Zakaria, R.; Alhomrani, M.; Alamri, A.S.; Alsanie, W.F.; Saied, E.M. New Mononuclear and Binuclear Cu(II), Co(II), Ni(II), and Zn(II) Thiosemicarbazone Complexes with Potential Biological Activity: Antimicrobial and Molecular Docking Study. *Molecules* **2021**, *26*, 2288. [[CrossRef](#)]
31. Wilson, J.T.; Jiang, X.; McGill, B.C.; Lisic, E.C.; Deweese, J.E. Examination of the Impact of Copper(II)  $\alpha$ -(N)-Heterocyclic Thiosemicarbazone Complexes on DNA Topoisomerase I $\alpha$ . *Chem. Res. Toxicol.* **2016**, *29*, 649–658. [[CrossRef](#)]
32. Conner, D.; Medawala, W.; Stephens, M.T.; Morris, W.H.; Deweese, J.E.; Kent, P.L.; Rice, J.J.; Jiang, X.; Lisic, E.C. Cu(II) Benzoylpyridine Thiosemicarbazone Complexes: Inhibition of Human Topoisomerase II $\alpha$  and Activity against Breast Cancer Cells. *Open J. Inorg. Chem.* **2016**, *6*, 146. [[CrossRef](#)]
33. Lisic, E.C.; Rand, V.G.; Ngo, L.; Kent, P.; Rice, J.; Gerlach, D.; Papish, E.T.; Jiang, X. Cu(II) Propionyl-Thiazole Thiosemicarbazone Complexes: Crystal Structure, Inhibition of Human Topoisomerase II $\alpha$ , and Activity against Breast Cancer Cells. *Open J. Med. Chem.* **2018**, *8*, 30–46. [[CrossRef](#)]
34. Sarker, D.; Hossen, M.F.; Zahan, M.K.; Haque, M.M.; Zamir, R.; Asraf, M.A. Synthesis, Characterization, Thermal Analysis and Antibacterial Activity of Cu (II) and Ni(II) Complexes with Thiosemicarbazone Derived from Thiophene-2-aldehyde. *J. Mater. Sci. Res. Rev.* **2020**, *5*, 15–25.
35. Mohan, C.; Kumar, V.; Kumari, S. synthesis, characterization, and antibacterial activity of schiff bases derived from thiosemicarbazide, 2-acetylthiophene and thiophene-2-aldehyde. *Int. Res. J. Pharm.* **2018**, *9*, 153–158. [[CrossRef](#)]
36. Tyagi, M.; Chandra, S.; Tyagi, P. Mn(II) and Cu(II) complexes of a bidentate Schiff's base ligand: Spectral, thermal, molecular modelling and mycological studies. *Spectrochim. Acta A Mol. Biomol. Spectrosc.* **2014**, *117*, 1–8. [[CrossRef](#)] [[PubMed](#)]
37. Chandra, S.; Goel, S.; Dwivedi, S.D. spectroscopic and biological studies on newly synthesized copper(II) and nickel(II) complexes with p-dimethylaminobenzaldehyde semicarbazone and p-dimethylaminobenzaldehyde thiosemicarbazone. *Int. J. Appl. Biol. Pharm.* **2012**, *3*, 149–156.
38. El-Saied, F.; El-Aarag, B.; Salem, T.; Said, G.; Khalifa, S.A.M.; El-Seedi, H.R. Synthesis, Characterization, and In Vivo Anti-Cancer Activity of New Metal Complexes Derived from Isatin-N(4) antipyrinethiosemicarbazone Ligand Against Ehrlich Ascites Carcinoma Cells. *Molecules* **2019**, *24*, 3313. [[CrossRef](#)]
39. Pahontu, E.; Fala, V.; Gulea, A.; Poirier, D.; Tapcov, V.; Rosu, T. Synthesis and Characterization of Some New Cu(II), Ni(II) and Zn(II) Complexes with Salicylidene Thiosemicarbazones: Antibacterial, Antifungal and in Vitro Antileukemia Activity. *Molecules* **2013**, *18*, 8812–8836. [[CrossRef](#)]
40. Jing, M.; Li, F.; Chen, M.; Zhang, J.; Long, F.; Jing, L.; Lv, X.; Ji, X.; Wu, T. Facile synthetic strategy to uniform Cu<sub>9</sub>S<sub>5</sub> embedded into carbon: A novel anode for sodium-ion batteries. *J. Alloys Compd.* **2018**, *762*, 473–479. [[CrossRef](#)]
41. Mbewana-Ntshanka, N.G.; Moloto, M.J.; Mubiayi, P.K. Antimicrobial Activity of the Synthesized of Copper Chalcogenide Nanoparticles. *J. Nanotechnol.* **2021**, *2021*, 6675145. [[CrossRef](#)]

42. Onwudiwe, D.C.; Hrubaru, M.; Ebenso, E.E. Synthesis, Structural and Optical Properties of TOPO and HDA Capped Cadmium Sulphide Nanocrystals, and the Effect of Capping Ligand Concentration. *J. Nanomater.* **2015**, *9*, 143632. [[CrossRef](#)]
43. Akhtar, M.; Alghamdi, Y.; Akhtar, J.; Aslam, Z.; Revaprasadu, N.; Malik, M.A. Phase controlled synthesis of copper sulfide nanoparticles by colloidal and non-colloidal methods. *Mater. Chem. Phys.* **2016**, *180*, 404–412. [[CrossRef](#)]
44. Ketchemen, K.I.Y.; Mlowe, S.; Nyamen, L.D.; Ndifon, P.T.; Revaprasadu, N. Comparative study on the effect of precursors on the morphology and electronic properties of CdS nanoparticles. *Turk. J. Chem.* **2021**, *45*, 400–409. [[CrossRef](#)]
45. Botha, N.L.; Ajibade, P.A. Optical and structural characterization of copper sulphide nanoparticles from copper(II) piperidine dithiocarbamate. *Opt. Quantum Electron.* **2020**, *52*, 337. [[CrossRef](#)]
46. Mintcheva, N.; Gicheva, G.; Panayotova, M.; Kulinich, S.A. Room-Temperature Synthesis of ZnS Nanoparticles Using Zinc Xanthates as Molecular Precursors. *Materials* **2020**, *13*, 171. [[CrossRef](#)]
47. Ajibade, P.A.; Sikakane, B.M.; Botha, N.L.; Oluwalana, A.E.; Omondi, B. Synthesis and crystal structures of bis(dibenzyl dithiocarbamate)Cu(II) and Ag(I) complexes: Precursors for Cu<sub>1.8</sub>S and Ag<sub>2</sub>S nano-photocatalysts. *J. Mol. Struct.* **2020**, *1221*, 128791. [[CrossRef](#)]
48. Pal, M.; Mathews, N.R.; Sanchez-Mora, E.; Pal, U.; Paraguay-Delgado, F.; Mathew, X. Synthesis of CuS nanoparticles by a wet chemical route and their photocatalytic activity. *J. Nanoparticle Res.* **2015**, *17*, 301. [[CrossRef](#)]
49. Yepseu, A.P.; Isac, L.; Nyamen, L.D.; Cleymand, F.; Duta, A.; Ndifon, P.T. Optical and Photocatalytic Properties of Cu<sub>x</sub>S/ZnO Composite Thin Films Deposited by Robotic Spray Pyrolysis Deposition. *J. Nanomater* **2021**, *2021*, 9975600. [[CrossRef](#)]